Characteristics and Provenance of High Content Volcanogenic Compositions in Shanxi Formation of Daniudi Gas Field, Ordos Basin and Tectonic Implications

Xuejiao Qu , Qiao Wang , Tao Lei , Hao Chen , Jia Wang , Wei Jiang , Wei Zhang , Long Luo , Jianping Liu , Nan Jiang , Xuanbo Gao , Xianfeng Tan *

Posted Date: 5 October 2023

doi: 10.20944/preprints202310.0258.v1

Keywords: volcanogenic compositions; provenance; tectonic evolution; Shanxi Formation; Ordos Basin

minerals

MDPI

Article

Characteristics and Provenance of High Content Volcanogenic Compositions in Shanxi Formation of Daniudi Gas Field, Ordos Basin and Tectonic Implications

Xuejiao Qu [1], Qiao Wang [1], Tao Lei [2], Hao Chen [3,4], Jia Wang [1], Wei Jiang [1], Wei Zhang [1], Long Luo [1], Jianping Liu [1], Nan Jiang [1,5], Xuanbo Gao [1] and Xianfeng Tan [1]*

[1] School of Petroleum Engineering, Chongqing University of Science and Technology, Chongqing 401331, China
[2] Exploration and Development Research Institute of North China Branch Company, SINOPEC, Zhengzhou 450006, China
[3] Chongqing 208 Geoenvironmental Engineering Survey and Design Institute Co., Ltd., Chongqing 401121, China
[4] College of Earth Sciences Chengdu University of Technology, Chengdu 610059, China
[5] School of Geoscience and Technology, Southwest Petroleum University, Chengdu 610500, China
* Correspondence: xianfengtan8299@163.com

Abstract: The detrital compositions in sandstone are important recorders of sedimentary provenance and transport, both of which have significant implications for the lithology, age and tectonic evolution of provenance. Through detailed identification and analysis, a high content of volcanogenic compositions (27.6%) was discovered in Shanxi formation of Daniudi Gas Field, Ordos Basin, which is much higher than that of the previous study. The volcanogenic compositions include volcanogenic quartz, lava fragments (dominated by various kinds of rhyolite fragments), tuff fragments, and tuffaceous matrix. In addition, at least 2 volcanic ash layers were discovered. Although the metamorphic rocks of the Precambrian succession in the ancient land of Yin Mountain are usually considered the primary source of the Shanxi formation, it is most likely that the volcanogenic compositions were derived from intermediate-acidic volcanic materials that accumulated in the Daqingshan area during the Late Carboniferous to Early Permian. Those volcanogenic compositions are mainly transported by flowing water rather than by air from provenance to basin. And the accumulation of volcanic materials in the Daqingshan area was controlled by volcanic eruptions occurring solely in this area, rather than by the Inner Mongolia Orogenic Belt. Those volcanic eruptions related to the southward subduction of the Paleo-Asian Ocean Plate beneath the northern margin of the North China Plate in Late Carboniferous to Early Permian. The active continental margin related to the subduction of the Paleo-Asian Ocean Plate lasted until at least the Early Permian, and the closure of the Paleo-Asian Ocean must have occurred later than the Early Permian.

Keywords: volcanogenic compositions; provenance; tectonic evolution; Shanxi Formation; Ordos Basin

1. Introduction

The Ordos Basin is a huge intracratonic basin located in the western margin of the North China Plate, spanning 28×10^4 km^2 (Figure 1a) [1,2]. It is bordered to the north by the Xing-Meng Orogenic Belt (Figure 1b) [3,4], which has experienced multi-stage oceanic plate subduction, crustal accretion and multi-block amalgamation among the North China Plate, Paleo-Asian Ocean Plate and south of Siberia Plate since the Early Paleozoic [5–8]. During the Shanxi Formation stage (Early Permian), continental clastic rocks accumulated in the north of the basin as the result of intense tectonic activity in the Xing-Meng Orogenic Belt [9–13]. However, petrographic data on sandstones deposited in intracratonic or epicratonic basins provide noteworthy information about provenance composition and geotectonic setting [14–20]. The continental clastic rocks of the Shanxi Formation in Daniudi Gas Field, located in the north of Ordos Basin, can help us better understand the lithology, age of provenance, and tectonic evolution of the Xing-Meng Orogenic Belt.

Previous workers have documented that the provenance of Shanxi Formation in Daniudi Gas Field was attributed to active recycled-orogenic provenance, and the source rock derived from metamorphic rock of Precambrian succession in the ancient land of Yin Mountain in the north of the Ordos Basin, and mixed with granite and alkaline basalt [9,10,12,13,21]. However, the high content of volcanogenic compositions (average over 27.6%) discovered recently in Shanxi Formation have raised questions that the previous research could not fully address. Their characteristics, provenance, and transportation have not been thoroughly analyzed. Furthermore, these volcanogenic compositions hold essential clues for understanding the evolution of the Xing-Meng Orogenic Belt and the closure of the Paleo-Asian Ocean, especially the debated subduction direction of the plate in the Xing-Meng Orogenic Belt [22–27].

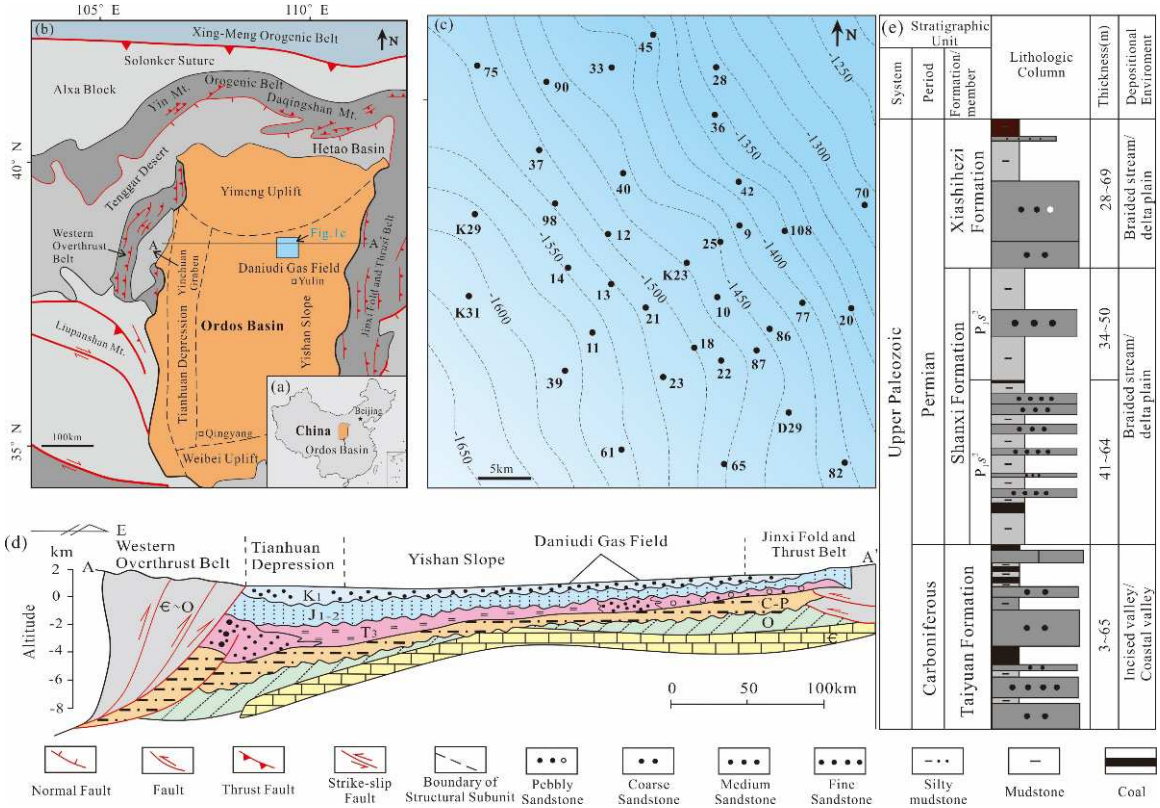

Figure 1. Location map and subtectonic units of the Ordos Basin and the Shanxi Formation stratigraphy. (a) Location of the Ordos Basin, China; (b) Locality map of Daniudi Gas Field showing the distribution of the main depressions and uplifts within and surrounding the Ordos Basin (modified from Darby & Ritts (2002) [55] and Xu et al. (2017) [56]; (c) Sampling well locations in Daniudi Gas Field; (d) Geologic structure cross section of the Ordos Basin (modified from Yang et al. (2005) [57]; (e) Upper Paleozoic stratigraphy for the region around Daniudi Gas Field.

In this work, we carried out a comprehensive study on the core of Shanxi formation in Daniudi Gas Field through core observation, thin section fine identification, scanning electron microscope (SEM) analysis, and cathode luminescence (CL) images analysis to determine the detail types and contents of volcanogenic compositions. Furthermore, we integrated the geochemical data obtained from fine-grained rocks with previous achievements. This allowed us to utilize petrographic data for characterizing the provenance and transport processes of the volcanogenic compositions. Additionally, the subduction direction of the plate in the Xing-Meng Orogenic Belt during the Late Carboniferous to Early Permian and the closure period of the Paleo-Asian Ocean were discussed.

2. Geological Setting

The Ordos Basin is a cratonic basin with multiple tectonic systems, multicyclonic evolution, and various sediment types [37–39]. The North China Plate (including Ordos Basin) is thought to have been deeply influenced by the closure of the Paleo-Asian Ocean during the Paleozoic [6,40,41]. During the late Early Paleozoic, an active continental margin with a trench-arc-basin system developed due to the southward subduction of an oceanic plate [42,43]. At the end of the Carboniferous period, the north part of Ordos Basin began to uplift due to the southward conjunction and

compression of Siberian Plate [44]. At the end of the Early Permian to Late Permian, the subduction tectonic setting transitioned to a collisional orogeny setting [12,45].

The Ordos Basin can be subdivided into six structural units: the Western Overthrust Belt, the Tianhuan Depression, the Yishan Ramp, the Jinxi Fold and Thrust Belt, the Yimeng Uplift, and the Weibei Uplift [46–51] (Figure 1b). The Daniudi Gas Field is situated in the northern part of the Yishan Ramp and characterized by few low-relief structures lacks faults (Figure 1b-c) [52]. After a nearly 130 Ma (Silurian and Devonian) absence of deposition, the basin began to accept deposition again in the late Carboniferous (Figure 1d). And the Early Permian Shanxi formation of Daniudi Gas Field is dominated by braided river delta plain deposits, which developed in the marine continental transitional environment [53,54]. The Shanxi Formation varies in thickness from 25 to 87 m and consists of 2 sub-members, P_1s^1 and P_1s^2 (Figure 1e). The P_1s^1 is further divided into 3 sub- members and 6 sub-layers, including P_1s^{1-1-1}, P_1s^{1-1-2}, P_1s^{1-2-1}, P_1s^{1-2-2}, P_1s^{1-3-1}, and P_1s^{1-3-2} in ascending order; and P_1s^1 is divided into 2 sub-members and 4 sub-layers, including P_1s^{2-1-1}, P_1s^{2-1-2}, P_1s^{2-2-1}, P_1s^{2-2-2} (Figure 1e). It mainly consists of grey medium-coarse sandstone, glutenite, conglomerate interbeded with black and dark grey mudstone, carbonaceous mudstone, as well as coal seams or coal lines developed in P_1s^1 (Figure 1e) [52].

3. Samples and Methods

This work was conducted using cores and 56 thin sections from 21 wells drilled in Shanxi Formation of Daniudi Gas Field (Figure 1c). The thin sections were impregnated with blue epoxy under a vacuum and stained with alizarin red-S and K-ferricyanide. Pure calcite is recognized by a pink stain, and ankerite by a blue stain.

Detailed core and thin section descriptions allow us to identify the fine compositions of tight sandstone. Thin section descriptions were performed using an Optec BK-POL Digital Polarizing Microscope under transmitted light, using both plane-polarized and cross-polarized light. Percentages of the detrital compositions, matrix, and cements were determined through at least 300 point counts per thin section.

22 samples were counted using ELM-3R-Leica DMLP Cathode Luminescence (CL) Microscope at the Craton Technology Co., Ltd., Beijing, for visual CL analyses. The resolution ratio and accuracy are estimated to be within 0.01mm for CL microscopy.

In order to characterize the morphologies and types of tuffaceous matrix, our study examined 11 samples. These samples were subjected to analysis using a JSM-7800F scanning electron microscope (SEM) equipped with energy-dispersive x-ray spectra (EDX). This analysis took place at the Chongqing Key Laboratory of Nano/Micro Composite Materials and Devices.

For the investigation of trace elements, a total of 9 samples were selected for analysis. These included 2 samples of tuffaceous mudstone, 2 samples of siltstone, 1 sample of silty mudstone, 1 sample of mudstone, 1 sample of coal and 2 samples of tuff. The analysis of trace elements was conducted by Craton Technology Co., Ltd., Beijing. The rock powers were first digested by HF+HNO_3 in Teflon bombs and analyzed with a ThermoFisher ICAP-RQ ICP-MS. The detailed sample-digesting procedure for ICP-MS analyses was followed by Zhang et al. (2012) [58]. Two standard rocks, GSR2 and GSR5, were chosen for calibrating element concentrations of the measured samples. The accuracy is estimated to be within 10% for trace elements.

4. Results

4.1. Petrological Characteristics

The results of core and thin-section observations indicate that the lithology of Shanxi Formation in Daniudi Gas Field predominantly consists of sandstone, mudstone, and coal, with occasional occurrences of conglomerate and tuff (Figure 2).

In the study area, the primary type of sandstone is litharenite, followed by lithic graywacke (Figure 3). The sandstone grain size exhibits significant variation, with the primary particle size distribution ranging from 0.4 to 1.4 mm. Furthermore, the particle rounding degree varies from subangular to angular (Figure 2e-j). The detrital compositions of glutenite is primarily composed of quartz and diverse lithic fragments (Table 1). Feldspar content is notably low, with most crystals having undergone kaolinization or replacement by calcite, ferroan calcite, or complete dissolution (Figure 2f). The lithic fragments include metamorphic, sedimentary and igneous rocks (Figure 2e, g-i). Metamorphic fragments are typically identified as slate, phyllite, metasandstone, schist, and dynamic metamorphic

rock. Sedimentary fragments predominantly originate from mudstone and sandstone, while igneous fragments are commonly characterized as intrusive rocks (predominantly granite) and extrusive rocks (dominated by rhyolite and tuff).

The matrix in this study can be classified into two primary types: terrigenous matrix and tuffaceous matrix (Table 1). The content of the tuffaceous matrix in the samples is relatively high and will be described in detail in the following sections. The cement is mainly composed of siliceous and calcareous cements (Table 1; Figure 2j), followed by clay minerals such as kaolinite, illite, and chlorite.

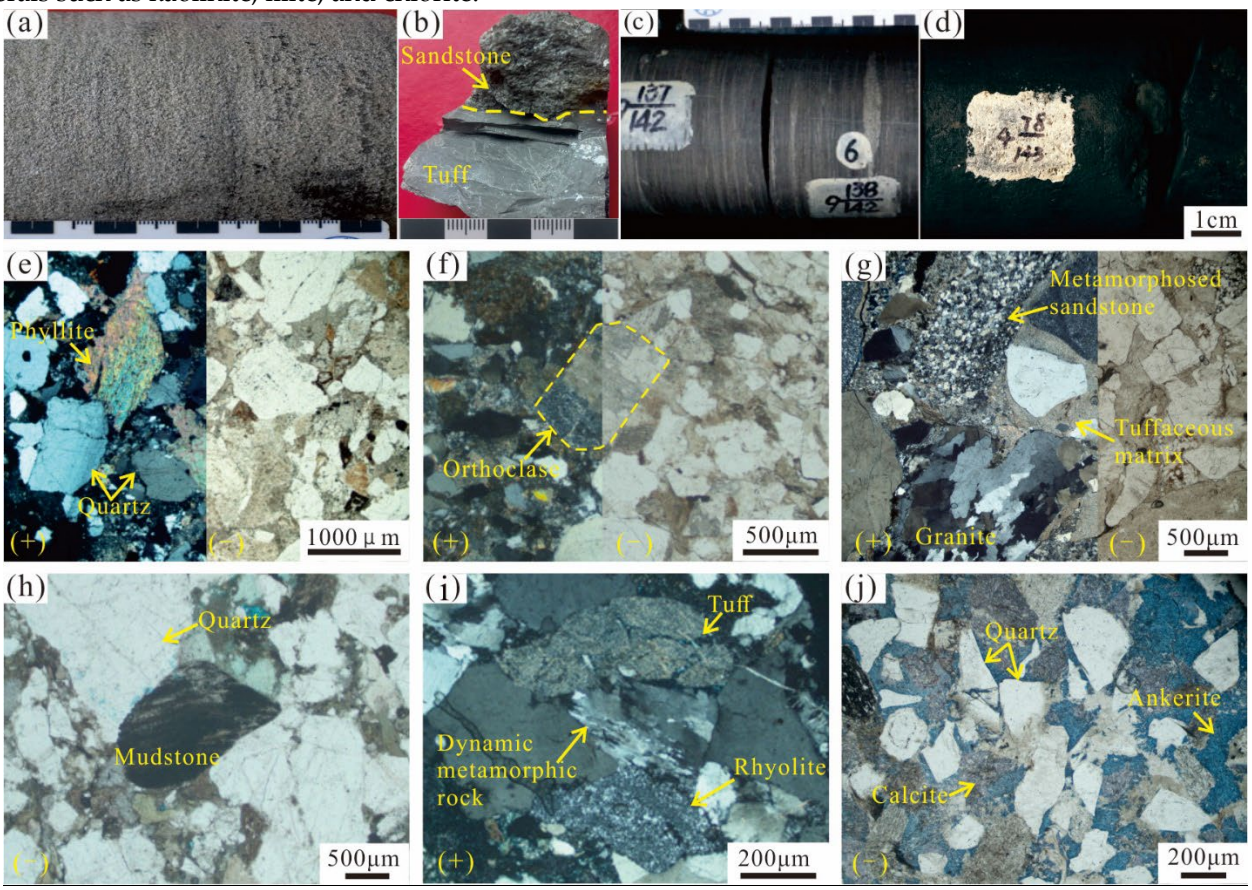

Figure 2. Petrological characteristics of Shanxi Formation in Daniudi Gas Field based on cores and thin sections. (a) Grey medium granular sandstone, parallel bedding, 13-2730.4 m; (b) Upper part is grey coarse granular sandstone, lower part is light grayish green tuff, 11-2699.0 m; (c) Dark grey mudstone with sandy banding, horizontal bedding, 10-2656.1 m; (d) Black coal, 42-2569.0 m; (e) Quartz and phyllite fragment, 44-2576.0 m; (f) Orthoclase metasomated by calcite, Carlsbad twin could be recognized, 39-2731.1 m; (f) Metamorphosed sandstone and granite fragment, tuffaceous matrix altered to sericite, 14-2812.5 m; (g) Quartz and mudstone fragment, 12-2789.1 m; (h) Dynamic metamorphic rock, rhyolite, tuff and granite fragment, sub-rounded quartz, 13-2706.0m, (i) Calcite metasomatism, ankerite cementation, angular quartz, 11-2701.2 m.

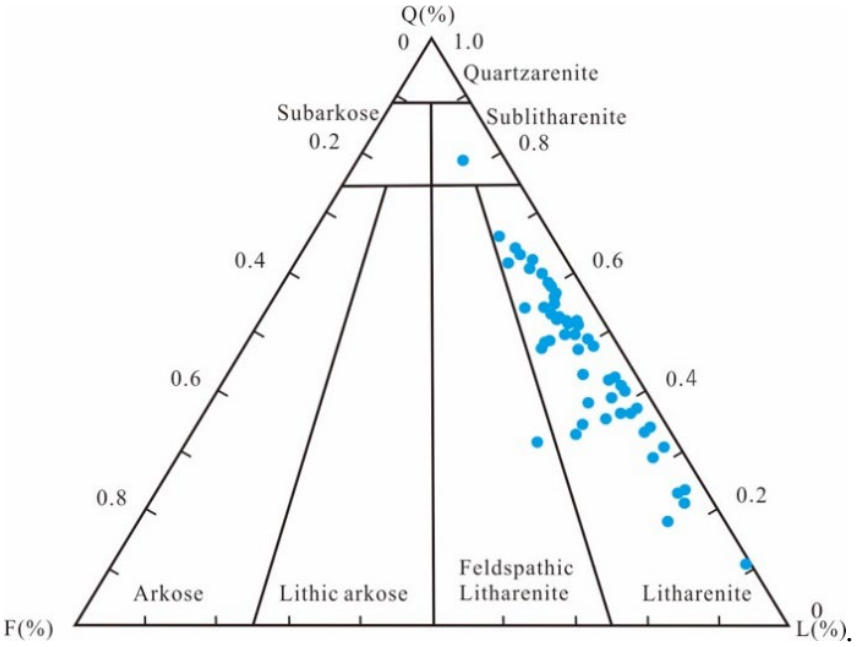

Figure 3. Sandstone composition of Shanxi Formation in Daniudi Gas Field [59].

Table 1. Percentages of detrital compositions , matrix, cements, and porosity for Shanxi Formation in Daniudi Gas Field (%).

						Lithic fragment										Matrix			Cement				
Well	Depth (m)	Quartz	Feldspar	Mica	Other minerals	Granite	Rhyolite	Basalt	Tuff	Slate	Phyllite	Schist	Metasand-stone	Dynamic metamorphic rock	Mudstone	Sandstone	Tuffaceous	Terrigenous	Ankerite	Ferroan calcite	Siliceous cement	Calcite	Argillanceous cement	Porosity (%)
12	2777.5	38				18	15		5	1			3	2	0.5		8	2			0.5		1	6
12	2772.2	45	2	1		4	12		15	1				2	2		10	2			0.5		1.5	2
12	2745.8	45				15	10		10				1		1		5	2	1		1		1	8
12	2745.0	50		1	0.5	8	5		8		1			1	2		15	3			1		3	1.5
12	2747.6	40				19	15		4				1	2	1		8	1		1	2		2	4
13	2792.0	48	1	1	2	4	10		7	1				1	4		12	2	2.5		0.5		1	3
13	2779.2	50		1		3	20		3			1		1	6	1	6	4			0.5		1.5	2
13	2775.6	31				22	20		5	0.5			5	2	3		4	2.5					3	2
13	2748.1	30	1			8	29		5	2			4				10	4	1		0		2	4
13	2732.2	15	5			30	13	0.5	5				3		2		6	2			1	8	1.5	8
13	2729.4	35				15	10		3				4	1	1		12	2			2		2	13
11	2798.8	30	2			20	10		4				3	3			8	2			0.5	1.5	3	13
11	2776.4	50				10	12		1	1			2	0.5			8	1	4		1.5	0	1	8
11	2728.8	36	2	0.5		8	15	1.5	10				2	3	3		8	4			0.5		2	4.5
11	2701.2	25	12	1	1	10	7	1.5	5	1	3		1	1	3		6	1	20				1	0.5
14	2812.5	30	1			20	15		3					1	2		15	2	1		1		2	7
14	2792.1	40	1			11	13		3				2				8	1	3	2	2		2	12
14	2775.2	40	4	1		3	5		15	1				1	2	0.5	10	3	8		0.5	2	1	3
10	2683.5	59	1	0.5		5	8		3	1			1	0.5	1		10	1	0.5		1	0.5	2	5

10	2659.8	43				8	5.5		8		3		2	1	2		12	2	5		1		1	6.5
10	2645.6	40	5		0.5	6	13		5	1			3		2		7	3	3	1	3		2	5.5
10	2679.6	43				12	15		3				1	2		3	8	0.5	1		1		0.5	10
9	2591.3	27	8	3	2	8	12	1	10	1		1		2	2		10	3		5	0.5		3	1.5
9	2570.7	30	7	1		8	13		5	1	3	2		2	3	2	5	3	2	7	1		3	2
9	2569.3	21	1			15	25	1	12	1			2		1		5	2	2	0	1	1	2	8
87	2697.3	60				5	10		4	1	1			1.5	1		9	2	1		0.5		1	3
87	2684.5	25	1			21	10		5					4			10	2			3	2	2	15
86	2626.5	54	1			5	7		2				4	1	3		10	2	2		3		2	4
86	2585.1	50	0.5	0.5		5	8		8	1	2			1	2		15	2			1		2	2
21	2665.6	35				20	15		2	1			5	2	1	1	10	1	1		0.5	0.5	1	4
21	2646.4	30			2	25	12		1				1	2	2	4	10	1.5	0.5		2		1	6
21	2602.6	35	5			15	9		8				4	2	2		3	3			1	5	2	6
22	2656.4	40	5.5			10	10		4	1					2	1	6	2			3.5	8	1	6
22	2654.9	40	2		1	12	5		5				3	2	1		13	2					1	13
25	2676.8	40	2			8	10		3					1			10	1	10		2		1	12
25	2596.9	65	2			1	7		8					1	1		4	2		3	1		2	3
24	2751.9	18	2			18	26		3				6	2			5	1	1	12	1	0	1	4
24	2708.3	50	2			6	10		6	1	1		2	2			10	3			1		3	3
31	2808.5	55		1		8	5.5		5					5	2	1	7	2			0.5		1	7
31	2802.6	40		1		10	14		5	1				1			10	2			1.5	0.5	2	12
108	2615.2	55	1			12	4		2	1			1	1			6	3	0.5		0.5		1	12
108	2548.3	45	2			5	12		6	0.5				1		2	12	2			0.5		2	10
18	2744.5	40				10	2		4	1	1						4	1.5	3	25	0	6	2	0.5
18	2696.1	45			1	5	10		8		2		4	2			10	6			2.5		3	1.5
18	2663.3	37	1			8	10		8		2		1		9		13	3.5			0.5		3	4
28	2619.7	25	2			15	22		3	2			4	3			10	3	2		1	2	1	5
28	2587.8	10				28	35		3.5		0.5		4	2			5	2			3		1	6
28	2562.9	30	4	1		13	15		8	2				2			8	3		5.5	0.5		3	5
94	2683.3	20	2			10	25	1	10	1			3	3		2	15	1			2.5		1.5	3

94	2669.1	35	3			19	8	1	3			2				8	2		5	2		1	11
40	2692.3	45	1			12	8		3			1	1	5		5	2			1		2	14
40	2679.1	50	2	3		3	12		10		2	1	1	2		6	2			1		2	3
1-4-1	2879.5	69				4	2						0.5			6	1.5			4		1	12

4.2. Volcanogenic Compositions

4.2.1. Volcanogenic Quartz

The quartz content ranges from 10% to 69% (average 39.3%) (Table 1). It should be noted that not all quartz is derived from the products of volcanic activity. The quartz is mainly derived from metamorphic rocks, sedimentary rocks, and igneous rocks in the provenance. And the authigenic quartz in the process of diagenesis could also be identified. The high-temperature magmatogenic quartz shows a blue-purple color in the CL image (Figure 3a), which can be used to distinguish it from other types of quartz. However, it is still hard to distinguish the volcanogenic quartz and intrusively original quartz for each particle. Still, some discriminant marks could be used to recognize the typical volcanogenic quartz, such as irregular shapes, angular in shapes, partly embayed boundaries or inward arc boundaries caused by high-temperature erosion, as well as rare abrasion marks caused by transportation (Figure 3b). The analysis of thin sections and CL images shows that the average volcanogenic quartz content is about 5%.

4.2.2. Lava fragment

The majority of the lava fragments are composed of rhyolite fragments, and sporadic basalt fragments could be found in a few thin sections. The lava fragment content varies from 2.0% to 29.0%, with an average of 11.5%. The rhyolite fragments display a complex texture and structure, allowing for the identification of various rhyolite types: (1) Rhyolitic structure rhyolite shows orientated range of crystallite and matted crystal without phenocryst (Figure 3c). (2) Amygdaloidal rhyolite, characterized by a lower degree of crystallinity and elongated vesicles filled with multi-stage quartz (Figure 3d). (3) Spherulitic rhyolite, displaying spherulitic textures of various shapes and sizes (0.1 to 0.6 mm) (Figure 3e). These spherulites come in two main types: one with a central nucleus surrounded by cyclic minerals and annular aphanitic felsic minerals, and the other with minimal or no central nucleus and radial felsic minerals around it. (4) Porphyroclastic rhyolite, featuring a porphyritic texture with varying degrees of matrix crystallization, ranging from aphanitic to fine-grained (Figure 3f). The phenocryst content is less than 3%, with most of the phenocrysts being quartz, and occasional feldspar phenocrysts that have fully dissolved. (5) Aphanitic, microcrystalline rhyolite, characterized by poorly crystallized felsic minerals without a typical rhyolitic structure, vesicles, spherulitic textures, or phenocrysts (Figure 3g). These may represent fragments of other rhyolites.

The basalt fragments contrast noticeably with the felsic fragments when viewed in plane-polarized light due to their darker appearance. In cross-polarized light, the basalt matrix exhibits a glass-based intersertal structure. Mafic minerals within the basalt have undergone alteration, resulting in the presence of chlorite, sericite, and other minerals.

4.2.3. Tuff fragment

The tuff fragment, derived from the consolidated volcanic ash in provenance and content, ranges from 1.0% to 15.0% (average 5.4%). The tuff fragment is mainly composed of volcanic ash, which has altered to sericite, kaolinite, and chlorite, or has been converted to felsic minerals by devitrification (Figure 3h). A few angular quartz crystals could be found in some tuff fragments (Figure 3h). The tuff fragments are characterized by semi-plastic deformation during strong compaction. Rigid particles, such as quartz and granite fragments, etc., are squeezed into the semi-plastic tuff fragments and are common in the tight sandstone of the Shanxi Formation (Figure 3h). Although they were easy to deform during strong compaction, the previous particle boundary of the tuff fragment can be identified (Figure 3h). This means that the intergranular pores wouldn't be fully filled with the deformed tuff fragments, which is significantly different from the tuffaceous matrix.

4.2.4. Tuffaceous matrix

The tuffaceous matrix is derived from unconsolidated volcanic ash, either from volcanic ash in the provenance or from fallout volcanic ash in the air. Its content ranges from 3.0% to 15.0% (with an average of 8.2%). The boundary of the tuffaceous matrix is amorphous and exhibits plastic deformation during strong compaction. The intergranular pores could be fully filled with the deformed tuffaceous matrix (Figure 3f, g, i-l), Called "pores fully filled" [60,61], which is similar to the deformation of soft sediments. Pores fully filled indicates that the tuffaceous matrix has never been compacted before being deposited with other clastic particles.

The tuffaceous matrix is colorless or light brown in plane-polarized light and can be divided into four types based on cross-polarized light and SEM analysis. Furthermore, the dissolution simulation experiment conducted by Wang et al. (2005) [60] and the burial history of the Upper Paleozoic in the Daniudi Gas Field, as completed by Yang et al. (2010) [1], could help us better understand the genesis of the four types of tuffaceous matrix. (1) Sericite, micro-scaly with a bright II~III order interference color (Figure 3f), formed in a closed diagenetic environment. In such conditions, the tuffaceous matrix remains relatively unaffected by dissolution, while its thermal evolution intensifies with increasing burial depth. The homogenization temperature of fluid inclusions ranges from 160°C to 170°C in some authigenic quartz in the Upper Paleozoic of Daniudi Gas Field [1]. The temperature is very close to very low-grade metamorphism, and the tuffaceous matrix is converted to sericite through metamorphic recrystallization. (2) Fine felsic minerals, in a closed condition, the unstable amorphous volcanic ash will converted to crystalline felsic minerals, which shows weak optical characteristics without optical orientation in cross polarized light (Figure 3g). (3) Impure kaolinite, which formed in an open diagenetic environment, and the tuffaceous matrix underwent intense dissolution. The differentiation of various elements such as Si, Al, K, Na, and Ca depends on cationic reactivity. As a result, the tuffaceous matrix evolves into a mixture of kalinite and chlorite in SEM images, referred to impure kalinite in plane-polarized light (Figure 3i-j). (4) Pure kaolinite, which formed in a more open diagenetic environment, experiences the transport of Si and Al by diagenetic fluids to adjacent pores. Consequently, pure kaolinite is deposited (Figure 4k-l), and only a few instances of chlorite mixed with kaolinite were observed in pure kaolinite (Figure 4k-l).

4.2.5. Volcanic ash layers

At least 2 volcanic ash layers were discovered in the Shanxi Formation during core observation. These ash layers are embedded within sandstone and exhibit thicknesses ranging from 4 to 6 cm. They are light green-gray and feel exquisite and smooth (Figure 2b). Notably, these layers stand in stark contrast to the adjacent dark-colored mudstone interlayers, which appear predominantly black or dark grey. Additionally, there is an absence of observable sedimentary transport characteristics at the base of these volcanic ash layers. Thin section observation shows that the volcanic ash has been converted to sericite and various clay minerals.

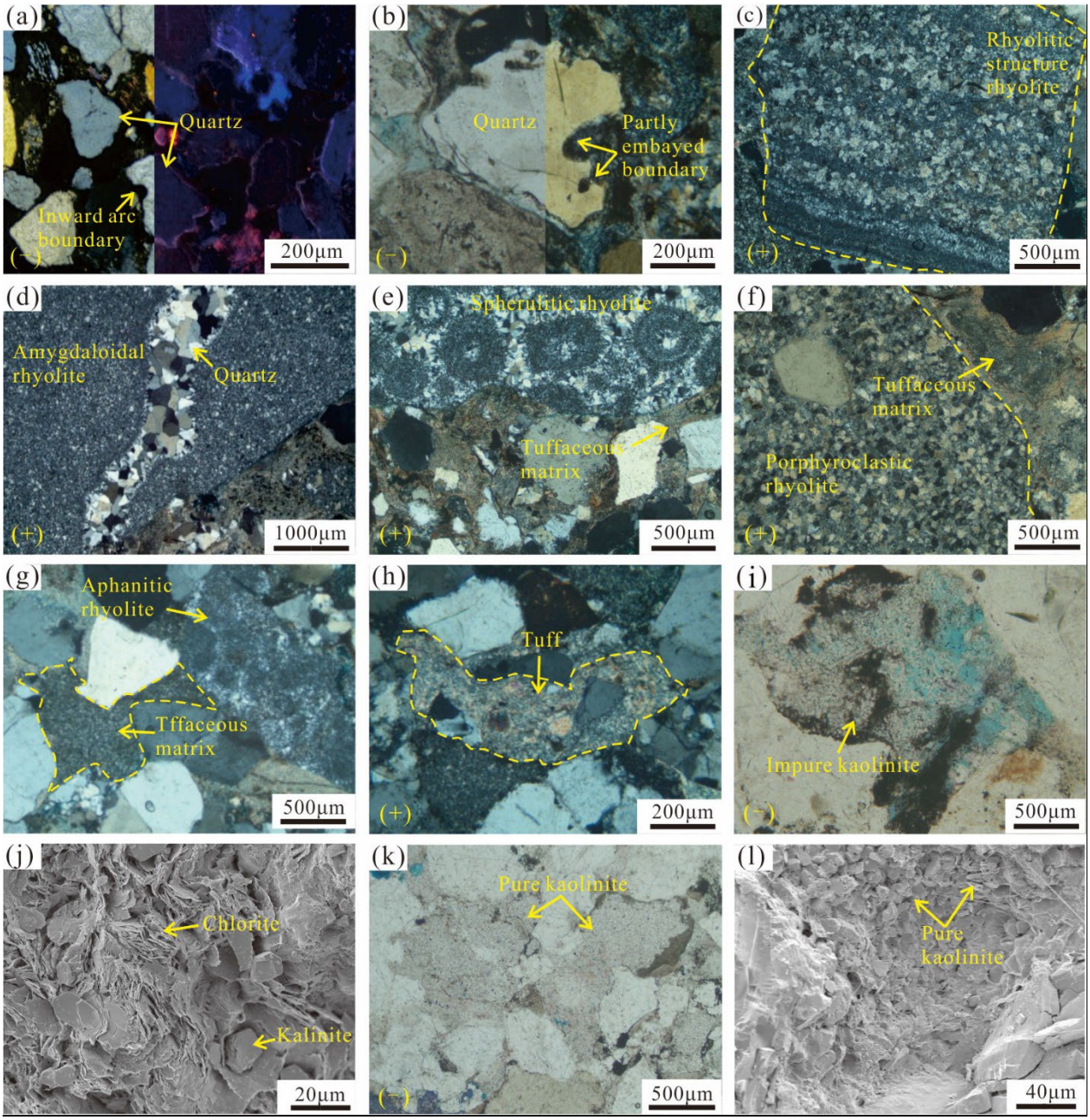

Figure 4. Photomicrographs of volcanogenic compositions in Shanxi Formation. (a) Quartz with inward arc boundary and shows blue-purple in CL image (right), 11-2725.9 m; (b) Quartz with partly embayed boundary, 24-2703.3 m; (c) Rhyolitic structure rhyolite fragment, 12-2787.8 m; (d) Amygdaloidal rhyolite fragment, elongated vesicle fully filled with multi-stages quartz, 14-2812.5 m; (e) Spherulitic rhyolite fragment, tuffaceous matrix **shows** "pores fully filled", 12-2779.5 m; (f) Porphyroclastic rhyolite fragment, tuffaceous matrix altered to sericite, 14-2812.5 m; (g) Aphanitic rhyolite fragment, tuffaceous matrix shows "fully filled pores" and converted to crystalline felsic minerals, 12-2787.8 m; (h) Tuff fragment with angular quartz crystal, 39-2734.3 m; (i) Impure kaolinite, 13-2729.4m; (j) Impure kaolinite, the mixture of kalinite and chlorite in SEM image, 13-2729.4m; (k) Pure kaolinite, 18-2686.0 m; (l) Pure kaolinite in SEM image, 18-2686.0 m.

4.3. Trace elements

The immobile trace elements in terrigenous clastic rocks, such as La, Th, Zr, Sc, and Co, etc., are characterized by relative high stability, which could be used to constrain the provenance and tectonic setting [62,63]. The results of trace element analysis are given in Table 2, and the Post-Archaean Average Shale (PAAS) normalized trace element spidergram [64] is shown in Figure 5.

The concentrations of the trace elements in the investigated fine-grained sedimentary rocks vary significantly. The content of high field strength elements (Zr, Hf, Y, Th, Nb, Ta) and transition trace elements (V, Cr, Co, Ni) ranges from 13 to 2707.4, 11 to 2784.0, and 87 to 2699.6, respectively, which is generally lower than that of PAAS. However, the concentrations in the remaining samples are higher than those in PAAS (Table 2; Figure 5). The content of Sc and La in most of the samples is higher than that of PAAS. In contrast, the content of large ion lithophile elements (LILE, Rb, Sr, Cs, Ba) is lower than that of PAAS (Table 2; Figure 5).

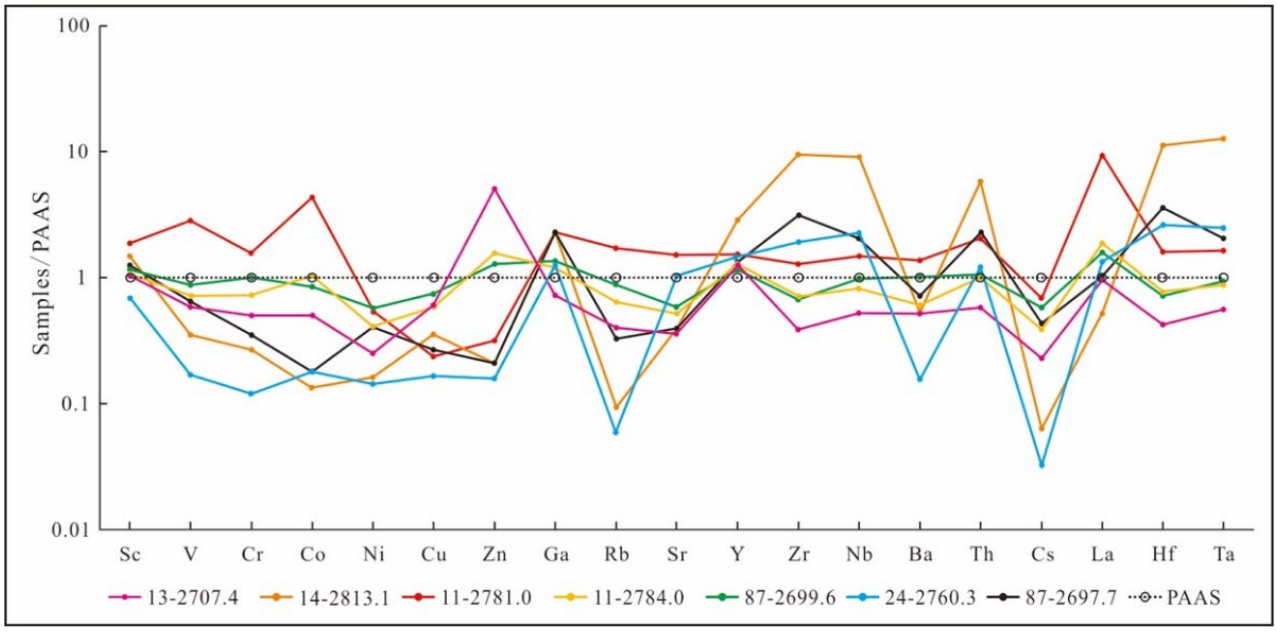

Figure 5. Trace elements spidergram of the investigated fine grained sedimentary rocks normalized to PAAS [64].

Table 2. Trace elements contents for the Shanxi Formation fine grained sedimentary rocks and tuff (μg/g).

Samples	13-2707.4	14-2813.1	11-2781.0	11-2784.0	87-2699.6	24-2760.3	87-2697.7	11-2699.0	24-2813.1
Lithology	**Tuffaceous mudstone**	**Tuffaceous mudstone**	**Siltstone**	**Siltstone**	**Mudstone**	**Silty-mudstone**	**Coal**	**Tuff**	**Tuff**
Li	22.94	157.84	7.46	35.99	56.01	154.48	206.95	29.59	7.46
Be	1.68	7.71	4.94	1.97	2.55	4.28	5.27	3.65	4.94
Sc	16.99	23.56	29.84	17.14	18.44	10.92	19.94	31.95	29.84
V	88.09	52.82	424.61	106.13	130.56	25.07	96.80	238.80	424.61
Cr	54.91	29.33	171.34	79.12	107.72	13.00	37.89	135.74	171.34
Co	11.64	3.09	98.94	23.69	19.43	4.12	4.09	32.03	98.94
Ni	13.69	8.82	29.70	22.38	31.25	7.80	22.01	35.18	29.70
Cu	29.90	17.67	11.79	28.86	36.98	8.26	13.27	8.43	11.79
Zn	426.84	17.79	26.63	132.55	108.81	13.36	17.70	98.53	26.63
Ga	14.38	45.76	45.66	23.73	27.09	24.84	44.88	53.01	45.66
Rb	63.57	14.96	272.92	102.10	139.91	9.40	51.99	184.70	272.92
Sr	71.28	77.42	299.29	103.47	117.42	204.48	79.18	298.25	299.29
Y	35.34	77.14	40.43	34.77	30.9	38.94	35.43	45.02	40.43
Zr	81.13	1970.04	268.05	147.08	139.58	404.01	656.74	396.11	268.05
Nb	9.87	170.95	28.14	15.44	18.63	42.99	39.07	56.18	28.14
Mo	0.18	1.92	0.16	0.42	0.44	1.27	0.70	0.27	0.16
Cd	1.55	0.00	0.03	0.35	0.26	0.03	0.01	0.03	0.03
In	0.16	0.32	0.12	0.11	0.11	0.15	0.22	0.11	0.12
Sb	0.12	0.65	1.12	0.32	0.25	0.24	0.11	0.25	1.12

Cs	3.42	0.94	10.18	5.74	8.68	0.48	6.48	7.38	10.18
Ba	308.30	316.38	814.12	361.45	611.65	92.72	427.08	537.82	814.12
Hf	2.11	55.57	7.98	3.85	3.56	12.91	17.87	11.03	7.98
Ta	0.71	16.21	2.10	1.11	1.19	3.16	2.60	3.02	2.10
W	20.51	15.68	37.11	46.62	11.30	15.47	6.39	14.47	37.11
Re	0.00	0.00	0.00	0.00	0.00	0.00	0.00	0.00	0.00
Tl	0.38	0.11	1.91	0.67	0.79	0.11	0.50	0.94	1.91
Pb	20.61	125.35	56.11	29.83	34.95	29.16	27.45	46.11	56.11
Bi	0.22	1.31	0.88	0.34	0.38	0.82	0.84	0.22	0.88
Th	8.46	84.56	29.70	14.49	15.62	17.69	33.09	39.11	29.70
U	1.95	8.53	9.95	2.97	3.16	6.50	6.90	8.83	9.95

4.4. Rare Earth Elements

The results of rare earth element (REE) analysis are given in Table 3. To better understand the possible provenances, the Chondrite-normalized REE patterns [64] are shown in Figure 6.

The total REE content in terrigenous clastic rocks (∑REE) varies from 167.20 μg/g to 1134.65 μg/g, with an average of 369.28 μg/g (Table 3). ∑REE is higher than that of the Upper Crust (UC, 146.37 μg/g) and the Post-Archaean Australian Shales (PAAS, 183.00 μg/g) [64]. Additionally, the ratio of (∑LREE/∑HREE) ranges from 2.38 to 28.48 (average 11.36) (Table 3), which is also higher than that of UC (9.54 μg/g) and PAAS (9.52 μg/g). Furthermore, the Eu anomaly (Eu/Eu*) varies between 0.44 and 0.69 (average 0.57) (Table 3). The distribution curves of LREE are relatively steep, while the curves of HREE are relatively flat (Figure 6a). These curves show an obvious "V" shape at Eu, indicating negative Eu anomalies (Figure 6a orange line). Finally, The ratio of (Ce/Ce^{*}) ranges from 0.91 to 1.16 (average 0.99), and shows regular variations in Ce anomalies (Table 3).

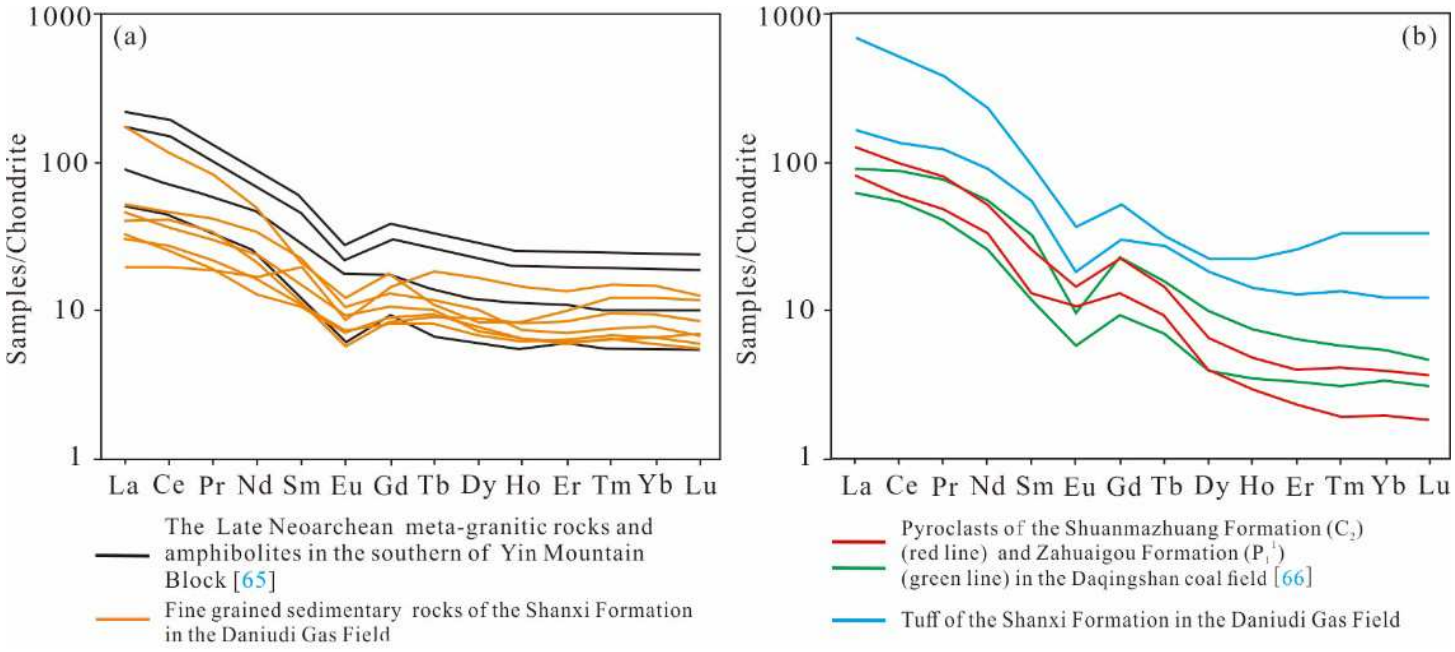

Figure 6. Chondrite normalized REE patterns of the investigated fine grained sedimentary rocks and tuff [64].

Table 3. Rare earth elements contents for the Shanxi Formation fine grained sedimentary rocks and tuff (μg/g).

Samples	13-2707.4	14-2813.1	11-2781.0	11-2784.0	87-2699.6	24-2760.3	87-2697.7	11-2699.0	24-2813.1
Lithology	Tuffaceous mudstone	Tuffaceous mudstone	Siltstone	Siltstone	Mudstone	Silty-mudstone	Coal	Tuff	Tuff
La	36.63	19.68	362.04	71.75	60.37	51.06	38.85	242.76	362.04
Ce	77.01	51.55	540.65	156.64	121.2	137.51	72.64	460.75	540.65
Pr	8.36	6.86	49.06	20.08	13.81	15.12	7.1	49.28	49.06
Nd	30.24	31.37	128.47	80.14	47.95	42.34	21.63	155.53	128.47
Sm	5.93	12.5	13.48	14.81	8.56	5.85	5.49	20.46	13.48
Eu	1.25	1.64	2.45	1.97	1.73	0.91	1.21	2.93	2.45
Gd	5.24	10.34	14.4	9.52	7.08	5.6	5.7	14.12	14.4
Tb	1	2.82	1.44	1.58	1.27	1.14	1.19	1.67	1.44
Dy	5.29	16.15	6.6	8.21	5.74	6.84	6.08	7.57	6.6
Ho	1.03	3.04	1.44	1.26	1.05	1.41	1.05	1.73	1.44
Er	3.12	8.2	5.38	3.4	2.78	4.33	2.75	5.93	5.38
Tm	0.49	1.34	1	0.54	0.48	0.74	0.44	1.06	1
Yb	3.11	8.98	7.2	3.87	3.09	5.02	2.7	7.52	7.2
Lu	0.49	1.14	1.03	0.48	0.43	0.67	0.39	1.16	1.03
La/Yb	11.79	2.19	50.26	18.52	19.54	10.18	14.38	32.29	50.26
∑REE	179.18	175.62	1134.65	374.25	275.53	278.51	167.20	972.48	297.84
∑HREE	19.76	52.01	38.50	28.87	21.92	25.74	20.29	40.76	24.81
∑LREE	159.42	123.61	1096.16	345.38	253.61	252.77	146.92	931.72	273.03
∑LREE/∑HREE	8.07	2.38	28.48	11.96	11.57	9.82	7.24	22.86	11.00
Eu/Eu*	0.69	0.44	0.54	0.51	0.68	0.48	0.66	0.53	0.44
Ce/Ce*	0.99	0.95	0.97	1.03	0.91	1.04	1.16	0.93	0.98
Ce_{anom}	0	-0.05	-0.02	0.01	-0.04	0	0.12	-0.03	0
Gd_N/Yb_N	1.37	0.93	1.62	1.99	1.86	0.90	1.71	1.52	2.51

Eu/Eu* and Ce_{anom} normalized by Chondrite and PAAS [64]; δEu (Eu/Eu*) = $(2Eu_N)/(Sm_N+Gd_N)$; $Ce_{anom} = \log_{10}[/3Ce_N/(2La_N+Nd_N)]$.

5. Discussion

5.1. Contradiction between the main provenance of Shanxi Formation and those volcanogenic compositions

The previous research achievements show that the provenance of the Shanxi Formation in Daniudi Gas Field was attributed to an active recycled-orogenic provenance and derived from metamorphic rocks of Precambrian succession in the ancient land of Yin Mountain in the north of the Ordos Basin [9,10,12,13,21]. Our own data further corroborates these conclusions: The Dickinson triplots show a recycled orogenic provenance (Figure 7a-b). The Rb and Ba content in the majority of terrigenous clastic rocks demonstrates depletion relative to PAAS (Table 2; Figure 5). It appears that Rb and Ba were flushed out from seawater by the incoming freshwater. As suggested by Norry et al. (1994) [67], these sediments might have undergone multiple cycles of weathering, erosion, and redeposition, potentially resulting in material being added or removed. The Chemical Index of Alteration (CIA) also indicates a strong weathered provenance, which ranges from 83.96 to 99.06 (average 91.65). The Chondrite-normalized REE patterns are consistent with those of the Upper Crust (UC) and also align with those of Late Neoarchaean (metamorphic) intrusive rocks such as amphibolite, plagioclase amphibolite schists, and tonalite, which are located in the southern part of the Yin Mountain Block [65] (Figure 6a). Additionally, the regular variations in Ce anomalies suggest a stable provenance supply (Table 3). The strong and varied concentrations of the trace elements among different samples imply that the provenance and tectonic setting are complex. The volcanic arc orogenic belt is one of them (Table 3; Figure 5), which is also supported by the Th-Sc-Zr/10 and La-Th-Sc plots (Figure 8). The complex and mixed provenance and tectonic setting of the Shanxi Formation include an active continental margin with subductional orogeny and a trench-arc-basin system.

However, the high content of unmetamorphosed volcanogenic compositions discovered in the Shanxi Formation in the Daniudi Gas Field can't be well explained by the previous research achievements. The Precambrian succession in the ancient land of Yin Mountain includes the Jining Group (Ar_{1-2}), Wulashan Group (Ar_3), Alashan Group (Ar_3-Pt_1), Sertengshan Group (Pt_1), Erdaowa Group (Pt_1^2), and Chaertaishan Group (Pt_2) in ascending order. Only minor and metamorphic volcanic rocks developed in the Alashan Group and Chaertaishan Group [11,68]. It was impossible for the fresh and unmetamorphosed volcanogenic compositions in the Shanxi Formation derived from the Precambrian basement, especially the easily metamorphosed tuffaceous matrix and tuff fragments. There must be a younger provenance consistent with the depositional period of Shanxi Formation, excluding the ancient basement. This implies that the volcanogenic quartz, lava fragments, tuff fragments, tuffaceous matrix, and volcanic ash layers must derived from volcanic eruptions that occurred earlier than or coeval with Shanxi Formation. One of the age peaks of detrital zircon is 301 Ma dated by Qu et al. (2020) [13] and another peak is 304 Ma dated by Chen (2020) [69], and the age of single-grain zircon, (295 ± 5) Ma, was also obtained by Chen (2020) [69] in the Shanxi Formation of the NE Ordos Basin. These zircon U-Pb ages are consistent with the depositional period of the Shanxi Formation (295-298 Ma) as reported by [70]. Moreover, a previous study shows that the content of Gd in old strata is relatively higher than in young strata for the fractionation of Gd, and the $(Gd/Yb)_N$ ratio could be used as a proxy for estimating the relative age of provenance [71]. In this regard, $(Gd/Yb)_N$ values in terrigenous clastic rocks fluctuate from 0.90 to 1.99, with an average of 1.48 (Table 3), while the value of Taiyuan Formation exceeds 2.00 [12]. The $(Gd/Yb)_N$ ratio indicates a decrease in the contribution from the old provenance (the ancient basement) and an increase from younger provenance from Taiyuan Formation to Shanxi Formation.

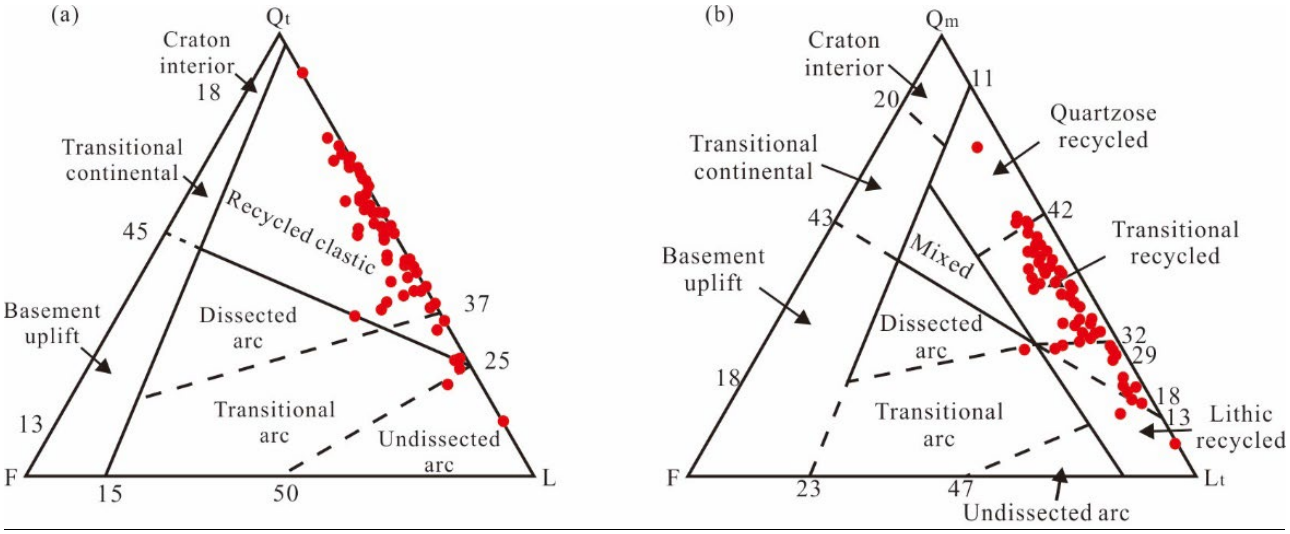

Figure 7. Provenance discrimination diagram of Shanxi Formation sandstones in Daniudi Gas Field [14,72].

Qt-Total quartzose grains, Qt=Qm+Qp; Qm-Monocrystalline quartz; Qp-Polycrystalline quartz; F-Total feldspar grains; L-Total unstable lithic fragments; Lt=L+Qp

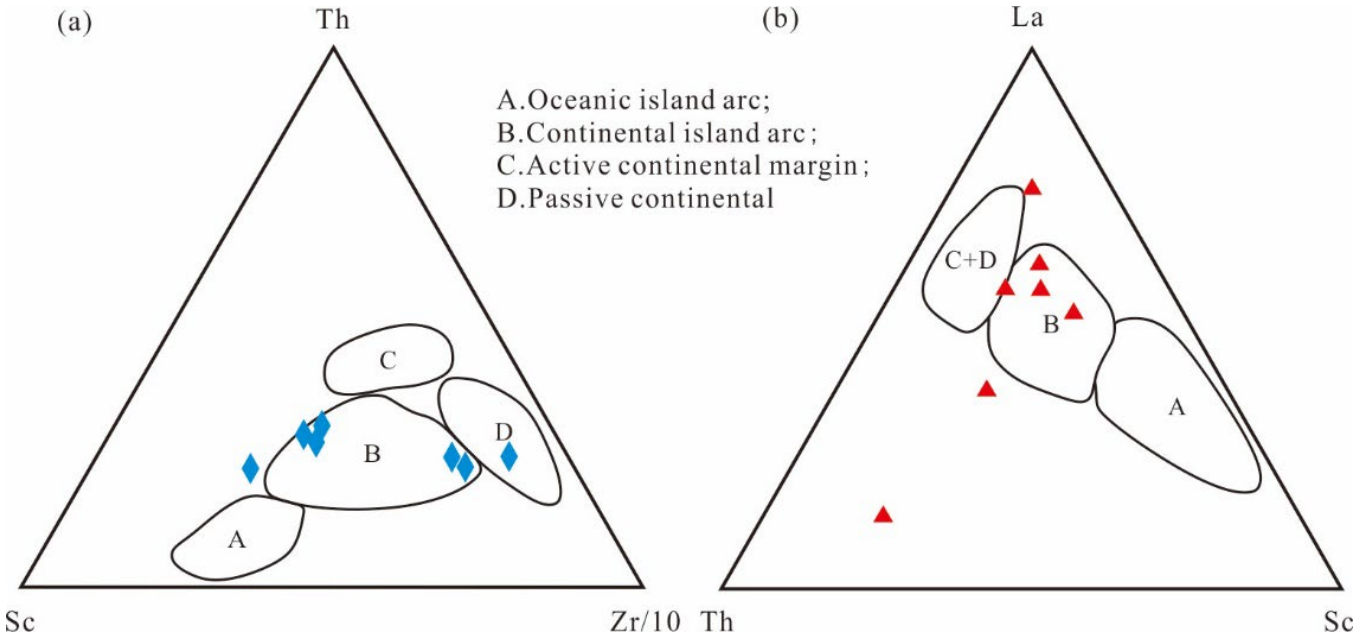

Figure 8. Discrimination diagrams of Th-Sc-Zr/10 (a) and La-Th-Sc (b) for the investigated fine grained sedimentary rocks [63].

5.2. Provenance and transportation of the volcanogenic compositions in Shanxi Formation

5.2.1. Provenance of the volcanogenic compositions

The Ordos Basin is located in the western part of the North China Plate, and there are few reports about the Late Paleozoic volcanic eruptions in the basin due to the absence of magmatic and tectonic activities. However, large-scale, multi-episode, Late Carboniferous to Early Permian intermediate-acidic volcanic eruptions were reported in the Inner Mongolia Orogenic Belt (part of the Xing-Meng Orogenic Belt), located to the north of the Ordos Basin (Figure 1b; Figure 9). The Baolige Temple (C_2), Tsagaannuur (C_2), Dashizhai (P_1), and Elitu (P_1) volcanic rock associations accumulated in the Inner Mongolia Orogenic Belt (Figure 9), with thickness ranging from 1 900 to 2 400 meters [73]. The Tsagaannuur and Baolige Temple volcanic rock associations mainly consist of rhyolite, dacite, andesite, which are distributed along the Sunit Right Banner-Linxi Tectonic Belt and East Ujimqin Banner Tectonic Belt (Figure 9) [13,73]. The isotopic age of these volcanic rocks mainly ranges from 320 Ma to 300 Ma and from 300 Ma to 290 Ma, which is consistent with the depositional period of the Shanxi Formation (295-298 Ma) [70]. The volcanogenic compositions in the Ordos Basin and North China Plate may be related to those volcanic eruptions.

However, it was implausible for the volcanogenic compositions in Shanxi Formation derived from the Inner Mongolia Orogenic Belt directly for the following reasons: 1) As mentioned previously, the provenance of the Shanxi Formation was mainly attributed to the Yin Mountain (Yinshan Orogenic Belt or Yin Mountain uplift), which is located between the Ordos Basin and the Inner Mongolia orogenic belt. The Yin Mountain uplift in the Late Paleozoic prevented the transportation of materials from the Inner Mongolia Orogenic Belt into the basin (Figure 9). 2) There is a considerable distance of approximately 400 to 600 km between the Daniudi Gas Field and the Sunit Right Banner-Linxi Tectonic Belt or the East Ujimqin Banner Tectonic Belt (Figure 9). Typically, sandstone with high compositional and structural maturity is conducive to long-distance transportation. Paradoxically, the predominant type of sandstone in the study area is litharenite, followed by lithic greywacke (Table 1; Figure 3), both of which contain a significant amount of lithic fragments and tuffaceous matrix (Figure 2c, g-i; Figure 4c-l). Furthermore, the presence of volcanogenic quartz with partly embayed boundaries or angular shapes suggests rapid sediment accumulation near the source (Figure 4a-b). 3) The Shanxi Formation in the Daniudi Gas Field is predominantly characterized by braided river delta plain deposits [53,54]. These deposits formed through a rapid accumulation process and were situated close to the provenance.

The most likely provenance of the volcanogenic compositions in Shanxi Formation is Daqingshan Mountain, which is located in the north of the Ordos Basin and is also situated in the middle of the Yinshan Mountain range (Figure 1b;

Figure 9). The Daqingshan coal field is situated on the southern slope of Daqingshan Mountain (Figure 9) and spans approximately 70 km from east to west and 1 to 10 km from south to north. Over 9 layers of volcanic event strata were discovered in the late Paleozoic coal-measure strata in Daqingshan coal field, mainly consisting of tufflava, volcanic breccia, ignimbrite, tuff, and sedimentary tuff (Figure 9) [66,74–76]. Notably, the total thickness of volcanic rock (excluding sedi-volcaniclastic rock and volcaniclastic sedimentary rocks) is approximately 42 m [74]. This finding suggests that a substantial amount of volcanic rock accumulated in the Daqingshan area, providing sufficient volcanic materials for the Daqingshan coalfield and the Shanxi Formation in the Ordos Basin. Moreover, the accumulation of intermediate-acidic volcanic materials in the Daqingshan area is consistent with the volcanogenic quartz, rhyolite fragments, tuff fragments, and tuffaceous matrix in Shanxi Formation. Meanwhile, the isotopic age of the volcanic rocks in the Daqingshan area is 305 Ma [76], which is also consistent with the depositional period of Shanxi Formation (295-298 Ma) [70]. In addition, the similar chondrite-normalized REE patterns of the tuff show that the Shanxi Formation has a strong affinity with the volcanic rocks in the Daqingshan area (Figure 6b). More importantly, the distance between the Daniudi Gas Field and the Daqingshan area is approximately 120 km, which is ideal for the rapid accumulation of a braided river delta plain (Figure 9). Based on the above considerations, we believe that the volcanogenic compositions in Shanxi Formation most likely derived from the Daqingshan area. The provenance of the Shanxi Formation in Daniudi Gas Field was derived not only from the ancient land of the Yin Mountain but also from the accumulation of Late Carboniferous to Early Permian intermediate-acidic volcanic materials in the Daqingshan area (Figure 10).

It is usually considered that the Late Carboniferous to Early Permian volcanic materials in the Daqingshan area mainly originated from volcanic eruptions in the Inner Mongolia Orogenic Belt and were transported through the air [23,66,77]. However, this study presents evidence of Late Carboniferous to Early Permian intermediate-acidic volcanic eruptions occurring directly within the Daqingshan area (Figure 10). Firstly, the timing of volcanic material accumulation in the provenance (Daqingshan area) can be constrained by the age peaks of detrital zircons (301 Ma and 304 Ma) in Shanxi Formation [13,27]. Furthermore, andesitic and dacitic tufflava containing 20% of various tephras, as well as volcanic breccia characterized by poorly sorted, subangular tephra of rhyolite, dacite, and andesite, have been discovered in the Daqingshan coal field [66,74–76]. Tufflava and lava breccia are the products of magma consolidation, which is close to the volcanic eruption centers. Additionally, the coarse volcanogenic quartz with partly embayed boundaries or angular shapes, as well as a coarse and high content of rhyolite fragments in the Shanxi Formation (Figure 4a-f), also implies that the intermediate-acidic volcanic eruption centers are located just in or close to the provenance.

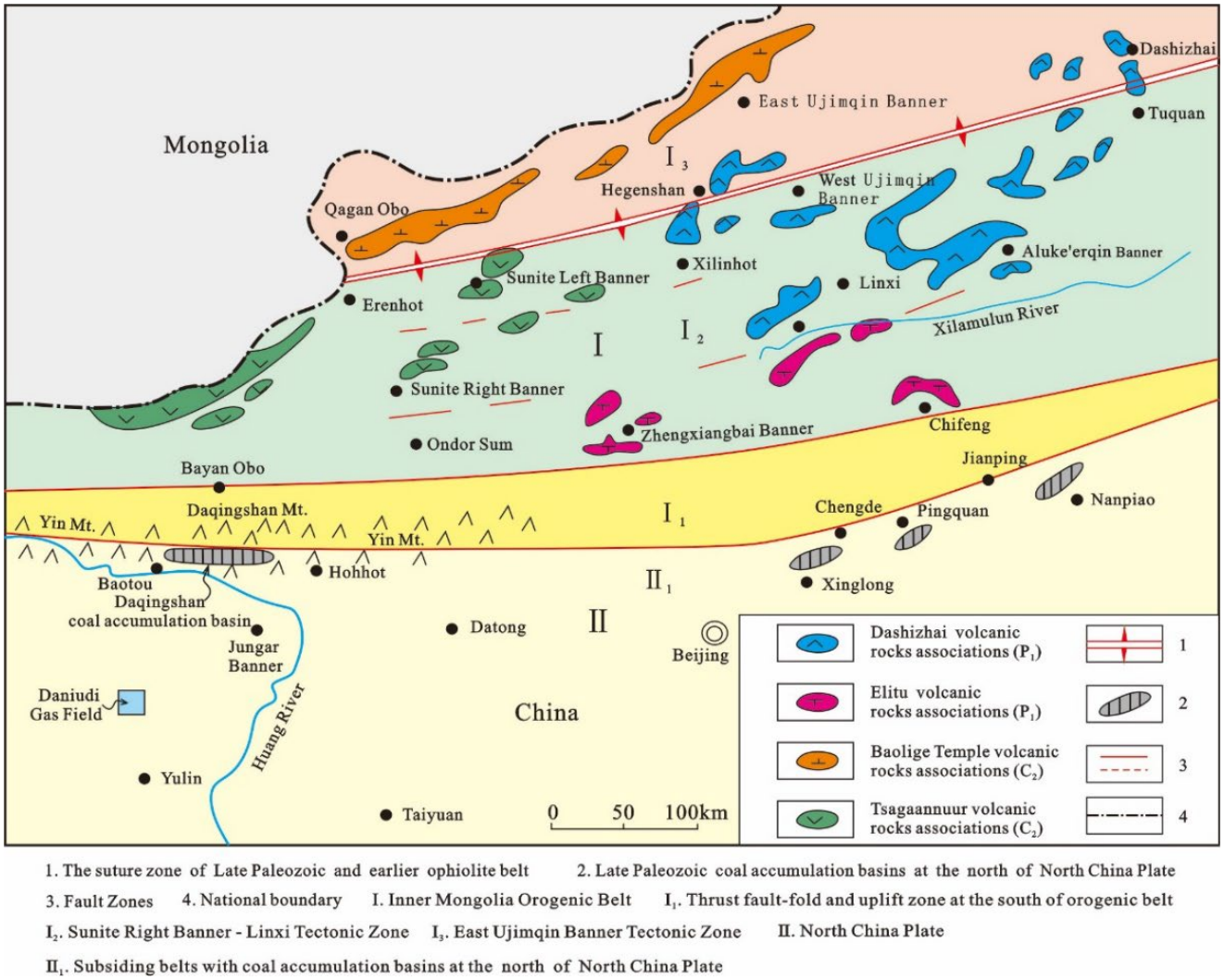

1. The suture zone of Late Paleozoic and earlier ophiolite belt 2. Late Paleozoic coal accumulation basins at the north of North China Plate
3. Fault Zones 4. National boundary I. Inner Mongolia Orogenic Belt I_1. Thrust fault-fold and uplift zone at the south of orogenic belt
I_2. Sunite Right Banner - Linxi Tectonic Zone I_3. East Ujimqin Banner Tectonic Zone II. North China Plate
II_1. Subsiding belts with coal accumulation basins at the north of North China Plate

Figure 9. The tectonic framework and Late Paleozoic volcanic rocks distribution in Inner Mongolia Orogenic Belt (modified after, Zhou, 2000 [23] and Bureau of Geology and Mineral Resources of Inner Mongolia Autonomous Region, 1991 [73]).

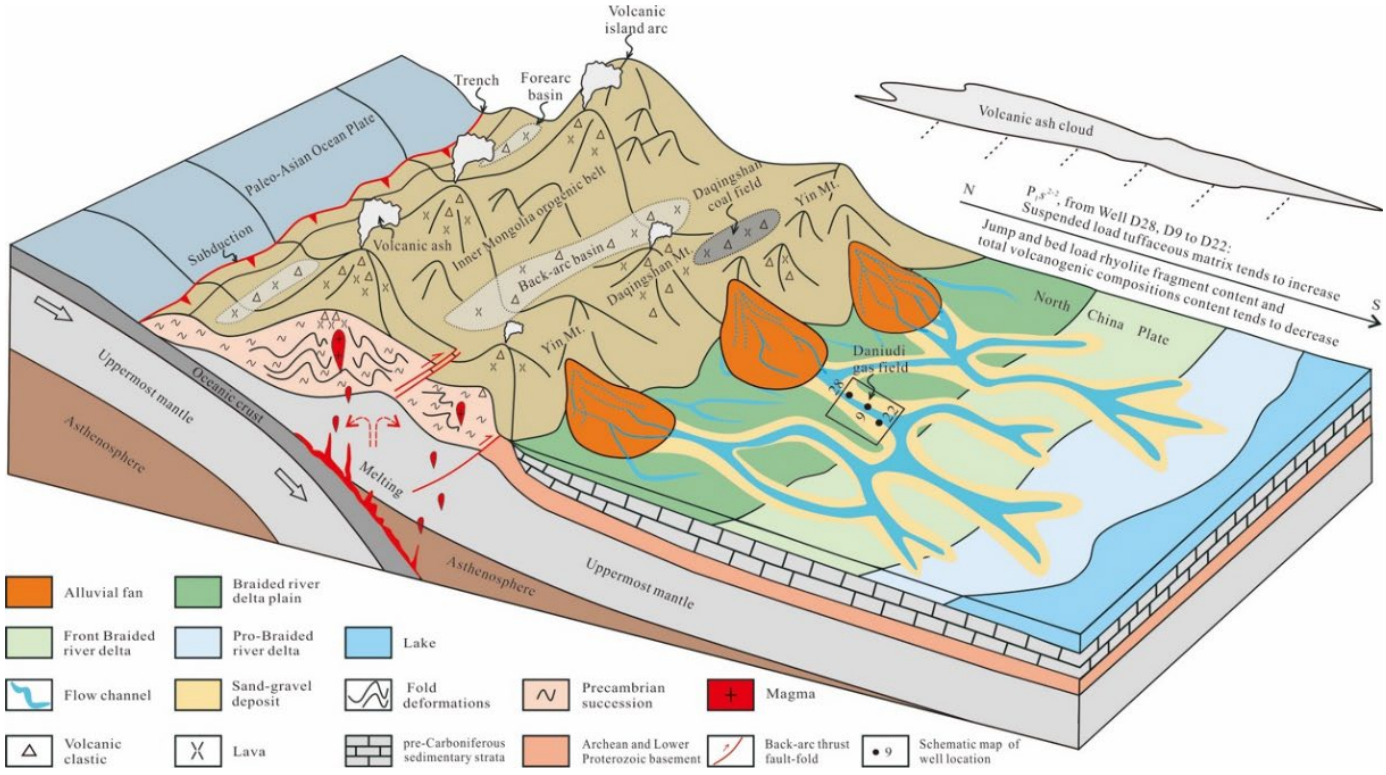

Figure 10. Tectonic-sedimentary model and provenance of Shanxi Formation in the north of Ordos Basin.

5.2.2. Transportation of the volcanogenic compositions

The volcanic ash layers in Shanxi Formation, which were transported by air, could be well explained by contemporaneous volcanic activities. However, air transportation could not well explain the high content of volcanogenic compositions in each sub-layer of Shanxi Formation (Table 4). The intermittent volcanic activities and relatively short residence time in the air of volcanogenic materials could not have continuously and stably contributed to the provenance of Shanxi Formation within 3 Ma for each sub-layer. Furthermore, the presence of coarse volcanogenic materials, such as coarse lava fragments exclusively in channels, and fine volcanogenic materials only could be found in flood plain, implies that these materials are primarily transported by flowing-water. Considering the paleocurrent directions of the Shanxi Formation in the study area, which were primarily from north to south or from northeast to southwest [78,79], the flowing-water transportation also could be proved by the variation of volcanogenic compositions content from north to south. Taking the P_1s^{2-2} as an example, the content of jump and bed load rhyolite fragments and the total content of volcanogenic compositions tend to decrease gradually, while the content of suspended load tuffaceous matrix tends to increase from Well 28 to Well 9 to Well 22 (Table 4; Figure 10). Therefore, these volcanogenic compositions in the Shanxi Formation were mainly transported by flowing water of alluvial fans and braided rivers rather than by air (Figure 10).

Table 4. Percentages of Volcanogenic compositions for each sub-layer and typical wells of Shanxi Formation in Daniudi Gas Field (%).

Sub-layer/ well	Samples	Rhyolite Fragment (%)			Tuff Fragment (%)			Tuffaceous Matrix (%)			Volcanogenic Compositions (%)		
		MIN	MAX	AVG	MIN	MAX	AVG	MIN	MAX	AVG	MIN	MAX	AVG
S2-2-2	5	5.0	10.0	8.2	4.0	8.0	6.0	3.0	13.0	8.0	12.0	31.0	22.2
S2-2-1	14	5.0	25.0	10.5	3.0	15.0	7.4	4.0	15.0	8.4	12.0	55.0	26.3
S2-1-2	2	13.0	15.0	14.0	5.0	10.0	7.5	7.0	8.0	7.5	25.0	33.0	29.0
S2-1-1	3	10.0	13.0	11.7	5.0	10.0	7.7	6.0	10.0	8.7	21.0	33.0	28.1
S1-3-2	5	5.5	18.0	12.7	3.0	15.0	7.0	5.5	12.0	8.7	14.0	45.0	28.4
S1-3-1	6	7.0	29.0	16.5	1.0	15.0	4.8	5.0	15.0	9.2	13.0	59.0	30.5
S1-2-2	4	8.0	15.0	11.3	1.0	5.0	2.8	8.0	10.0	9.5	17.0	30.0	23.5
S1-2-1	3	2.0	10.0	6.3	2.0	4.0	3.0	6.0	10.0	8.3	10.0	24.0	17.6
S1-1-2	2	10.0	20.0	15.0	4.0	5.0	4.5	4.0	8.0	6.0	18.0	33.0	25.5
S1-1-1	5	2.0	20.0	9.2	2.0	7.0	3.8	4.0	12.0	7.6	8.0	39.0	20.6
28	4	15.0	35.0	22.0	3.0	10.0	6.1	5.0	10.0	8.3	31.0	43.5	36.4
9	6	5.0	20.0	12.8	5.0	12.0	7.9	5.0	15.0	8.8	23.0	35.0	29.9
22	5	4.0	18.0	8.6	2.0	10.0	5.0	6.0	13.0	10.6	18.0	32.0	24.2

MIN: Minimum; MAX: Maximum; AVG:Average.

5.3. Tectonic Implications of High Content Volcanogenic Compositions in Shanxi Formation

The northern margin of the North China Plate is a key region for exploring the evolution of the Xing-Meng Orogenic Belt and the closure of the Paleo-Asian Ocean. The subduction direction of the plate in the Xing-Meng Orogenic Belt during the Late Carboniferous to Early Permian and the closure time of the Paleo-Asian Ocean are hotly disputed. Some scholars believe that the North China Plate subducted northward beneath the Southern Mongolian Microcontinent of the Siberia Plate [22–24], while others insist that the Paleo-Asian Ocean Plate subducted southward beneath the northern margin of the North China Plate [11,26,27,77,80]. In addition, it's argued that the Paleo-Asian Ocean closed in Late Devonian to Early Carboniferous [28–31] or Late Permian to Early Triassic [32–36]. The Late Carboniferous to Early Permian intermediate-acidic volcanic eruptions in the Daqingshan area could help us better understand the tectonic evolution of this area from a new point of view.

First of all, the Late Carboniferous to Early Permian intermediate-acidic magmatic activities could extend southward to the north margin of the North China Plate from the Inner Mongolia Orogenic Belt (Figure 9). The spatial distribution of magmatism related to the subduction of plates is no longer limited to the Inner Mongolia Orogenic Belt. However, it's important to note that the scale of magmatic activities significantly varies between the northern margin of the North China Plate and the Inner Mongolia Orogenic Belt. The thickness of the Tsagaannuur (C_2), Baolige Temple (C_2), and Dashizhai (P_1) volcanic rock associations in the Inner Mongolia Orogenic Belt is 1 990 ~ 2 089 m, ca. 2 400 m, and 1 150 ~ 2 000 m respectively [73]. While the total thickness of the Shuanmazhuang Formation (C_2), Zahuaigou Formation (C_2), and Shiyewan Zahuaigou Formation (C_2) in the Daqingshan area is 250 ~ 350 m, there are 39 layers of volcanic event deposits interbedded [23,66]. Clearly, the scale of magmatic activity in the Daqingshan area is much weaker than that in the Inner Mongolia Orogenic Belt, and the scale tends to decrease dramatically from north to south. This suggests that those volcanic activities triggered by the southward subduction of Paleo-Asian Ocean Plate, and the north of the North China Plate also be affected by the magmatic activities related to the subduction in Late Carboniferous to Early Permian. This conclusion is further supported by the Dickinson plots of clastic components in sandstones (Figure 7) and the plots of Th-Sc-Zr/10 and La-Th-Sc (Figure 8), which indicate an active continental margin with a trench-arc-basin system developed in the Late Carboniferous to Early Permian. Additionally, the high content of rhyolite and intermediate-acidic ash accumulated in the provenance is also more likely to be consistent with a volcanic island arc setting. Therefore, the active continental margin related to the subduction of the Paleo-Asian Ocean Plate lasted until at least the Early Permian, and the complete closure of the Paleo-Asian Ocean must have occurred later than the Early Permian.

6. Conclusions

(1) A high content of volcanogenic compositions was discovered in the Shanxi formation of Daniudi Gas Field, with average contents of volcanogenic compositions exceeding 27.6%. The volcanogenic compositions include volcanogenic quartz, lava fragments (dominated by various kinds of rhyolite fragments), tuff fragments, tuffaceous matrix, with average contents of approximately 5%, 11.5%, 5.4%, and 8.2%, respectively. In addition, at least 2 volcanic ash layers were discovered.

(2) The provenance of Shanxi Formation in Daniudi Gas Field was derived not only from the ancient land but also from much younger volcanic eruptions. The provenance primarily derived from the metamorphic rocks of the Precambrian succession in the ancient land of the Yin Mountains within an active recycled-orogenic setting. While the volcanogenic compositions most likely derived from intermediate-acidic volcanic materials accumulated in the Daqingshan area in the Late Carboniferous to Early Permian, they are earlier than or coeval with the Shanxi Formation. The volcanogenic

compositions in the Shanxi Formation were primarily transported by flowing water rather than by air from the provenance to the basin.

(3) The Late Carboniferous to Early Permian intermediate-acidic magmatic activities could have extended southward to the north margin of the North China Plate from the Inner Mongolia Orogenic Belt. The volcanic materials that accumulated in the Daqingshan area were associated with volcanic eruptions exclusive to this region. This phenomenon can be attributed to the southward subduction of the Paleo-Asian Ocean Plate beneath the northern margin of the North China Plate during the Late Carboniferous to Early Carboniferous period. The active continental margin related to the subduction of the Paleo-Asian Ocean Plate lasted until at least the Early Permian, and the closure of the Paleo-Asian Ocean must have occurred later than the Early Permian.

Author Contributions: Conceptualization, X.Q. and X.T.; methodology, X.Q. and X.C.; software, X.G.; validation, L.L., and W.J.; formal analysis, H.C.; investigation, X.Q., J.W. and H.C.; resources, T.L. and X.C.; data curation, B.T. and X.Q.; writing—original draft preparation, X.Q. and Q.W.; writing—review and editing, X.Q. and T.L.; visualization, J.N.; supervision, X.T.; project administration, X.T.; funding acquisition, X.Q. and X.T. All authors have read and agreed to the published version of the manuscript.

Funding: This work is supported by the National Natural Science Foundation of China (Grant Numbers. 42102135, 42102133), and Science and Technology Research Program of Chongqing Municipal Education Commission (Grant Numbers. KJQN202101535).

Conflicts of Interest: The authors declare no conflict of interest.

References

1. Yang, Z.; He, S.; Zou, C.N.; Li, Q.Y.; Chen, Z.Y. Coupling relationship between reservoir diagenesis and natural gas accumulation of Daniudi Gas Field in North Ordos Basin. *Acta Petrolei Sinica*. 2010, 31(3), 373-378, 385.
2. Wang, Z.; Zheng, M. Potash-forming regularity of the Ordovician marine northern Shaanxi salt basin: insight from review and prospect of the deep geology of the Ordos basin. *Acta Geologica Sinica*. 2018, 92 (4), 1627-1644.
3. Zhang, S.H.; Zhao, Y.; Song, B.; Yang, Z.Y.; Hu, J.M.; Wu, H. Carboniferous granitic plutons from the northern margin of the North China block: implications for a late Paleozoic active continental margin. *Journal of the Geological Society*. 2007, 164, 451-463.
4. Li, Z.H.; Qu, H.J.; Gong, W.B. Late Mesozoic basin development and tectonic setting of the northern North China Craton. *Journal of Asian Earth Sciences*. 2015, 114, 115-139.
5. Sengör, A.M.C.; Natal'in, B.A. Turkic-type orogeny and its role in the making of the continental crust. Annu. *Annual Review of Earth and Planetary Sciences*. 1996, 24, 263-337.
6. Windley, B.F.; Alexeiev, D.; Xiao, W.J.; Kröner, A.; Badarch, G. Tectonic models for accretion of the Central Asian Orogenic Belt. *Journal of the Geological Society*. 2007, 164, 31-47.
7. Jahn, B.; Brian, W.; Boris, N.; Nick, D. Phanerozoic continental growth in central Asia - Preface. *Journal of Asian Earth Sciences*. 2004, 23, 599-603.
8. Guo, F.; Fan, W.M.; Miao, L.C.; Zhao, L. Early Paleozoic subduction of the Paleo-Asian Ocean: Geochronological and geochemical evidence from the Dashizhai basalts, Inner Mongolia. *Science in China (Series D: Earth Sciences)*. 2009, 52(7), 940-951.
9. Liu, R.E.; Huang, Y.M.; Wei, X.F.; Sun, F.J.; Lin, J. Analysis of provenance of Late Paleozoic in the Northern Ordos Basin and its geological significance. *Journal of Mineralogy and Petrology*. 2003, 23(3), 82-86.
10. Chen, A.Q.; Chen, H.D.; Xiang, F.; Liu, W.J.; Hou, Z.J.; Shang, Y.Z.; Ye, L.M.; Li, H. Sandstone characteristic and provenance analysis of the Permian Shanxi Formation-Shangshihezi Formation in the northeast of Ordos Basin, China. *Journal of Chengdu University of Technology (Science & Technology Edition)*. 2007, 34(3), 305-311.
11. Chen, Q.H.; Li, W.H.; Liu, H.W.; Li, K.Y.; Pang, J.G.; Guo, Y.Q.; Yuan, Z. Provenance analysis of sandstone of the Upper Carboniferous to Middle Permian in Ordos Basin. *Journal of Palaeogeography*. 2009, 11(6), 629-640.
12. Chen, Q.H.; Li, W.H.; Hu, X.L.; Li, K.Y.; Pang, J.G.; Guo, Y.Q. Tectonic setting and provenance analysis of Late Paleozoic sedimentary rocks in the Ordos Basin. *Acta Geologica Sinica*. 2012, 86(7), 1150-1612.
13. Qu, H.J.; Han, X.; Chen, S.; Yang, B.; Du, M.Y.; Dong, Y.Y.; Zhao, C. U-Pb Dating of Detrital Zircon from the Upper Paleozoic Clastic Rocks and Basin-mountain Coupling of the Northeastern Ordos Basin. *Geotectonica et Metallogenia*. 2020, 44(3), 501-513.

14. Dickinson W.R.; Beard, S.; Brakenridge. R.; Erjavec, J.L.; Ferguson, R.C.; Inman, K.F.; Knepp, R.A.; Lindberg, A.; Ryberg, P.T. Provenance of North American Phanerozoic sandstones in relation to tectonic settings. *Geological Society of America Bulletin*. 1983, 94, 222-235.
15. Schieber, J. A combined petrographical-geochemical provenance study of the Newland Formation, mid-Proterozoic of Montana. *Geological Magazine*. 1992, 129, 223-237.
16. McCann, T. Sandstone composition and provenance of the Rotliegend of the NE German Basin. *Sedimentary Geology*. 1998, 116, 177-198.
17. Condie, K.C.; Lee, D.; Farmer, L. Tectonic setting and provenance of the Neoproterozoic Uinta Mountain and Big Cottonwood groups, northern Utah: constraints from geochemistry, Nd isotopes, and detrital modes. *Sedimentary Geology*. 2001, 141-142, 443-464.
18. Arribas, J.; Alonso, A.; Mas, R.; Tortosa, A.; Rodas, M.; Barrenechea, J.; Alonso-Azcárate, J.; Artigas, R. Sandstone petrography of continental depositional sequences of an intraplate rift basin: western Cameros Basin (North Spain). *Journal of Sedimentary Research*. 2003, 73, 309-327.
19. Osae, S.; Asiedu, D.K.; Banoeng-Yakubo, B.; Koeberl, C.; Dampare, S.B. Provenance and tectonic setting of late Proterozoic Buem sandstones of southeastern Ghana: Evidence from geochemistry and detrital modes. *Journal of African Earth Sciences*. 2006, 44, 85-96.
20. Ciccioli, P.L.; Limarino, C.O.; Isbell, J.L.; Taboada, A.C.; Pagani, M.A.; Gulbranson, E.L. Interpreting detrital modes and geochemistry of sandstones from the late Paleozoic Tepuel-Genoa Basin: Paleogeographic implications (Patagonia, Argentina). *Journal of South American Earth Sciences*. 2020, 104, 1-26.
21. Tan, C.X.; Li, W.H.; Feng, J.P.; Zeng, M.; Bu, Y. Analysis of sedimentary source of reservoir in Daniudi Gas Field in Ordos Basin. *Acta Mineralogica Sinica*. 2010, 30(3), 389-397.
22. Shang, G.X. An outline of basining structures of North China Late Palaeozoic coal accumulation basin. *Coal Geology of China*. 1995, 30(7), 1-6, 17.
23. Zhou, A.C. *The evolution of Late Paleozoic basins in north margin of North China Block and the coupling relationship between basin and range*; Northwestern University: Xi'an, China, 2000.
24. Shao, J.A.; Tang, K.D.; He, G.Q. Early Permian tectono-palaeogeographic reconstruction of Inner Mongolia, China. *Acta Petrologica Sinica*. 2014, 7(2), 1858-1866.
25. Chen, B.; Jahn, B.M.; Tian, W. Evolution of the Solonker suture zone: Constraints from zircon U–Pb ages, Hf isotopic ratios and whole-rock Nd–Sr isotope compositions of subduction- and collision-related magmas and forearc sediments. *Journal of Asian Earth Sciences*. 2009, 34, 245-257.
26. Zhao, Y.; Zhai M.G.; Chen H.; Zhang S.H. Paleozoic-Early Jurassic tectonic evolution of North China Craton and its adjacent orogenic belts. *Geology in China*. 2017, 44(1), 44-60.
27. Chen, A.Q.; Zhou H.; Ogg, J.G.; Yang, S.; Hou, M.C.; Jiang, X.W.; Xu S.L.; Zhang X.X. Source-to-sink of Late carboniferous Ordos Basin: Constraints on crustal accretion margins converting to orogenic belts bounding the North China Block. *Geoscience Frontiers*. 2020, 11, 2031-2052.
28. Xu, B.; Chen, B. The structure and evolution of Paleozoic -Mesozoic orogenic belt between North China Plate and Siberian Platein northern Inner Mongolia. *Science in China (Series D)*. 1997, 27(3): 227-232.
29. Shao, J.A.; Tian, W.; Tang, K.D. Petrogenesis and tectonic settings of the Late Carboniferous high Mg basalts of Inner Mongolia. *Earth Science Frontiers*. 2015, 22(5): 171-181.
30. Zhu, J.B.; Ren, J.S. Carboniferous–Permian Stratigraphy and Sedimentary Environment of Southeastern Inner Mongolia, China: Constraints on Final Closure of the Paleo-Asian Ocean. *Acta Geologica Sinica*. 2017, 91(3): 832-856.
31. Tong, Y. Giant late Carboniferous-early Permian alkaline granite belt along the China and Mongolia Border and its implication for the evolution of the CAOB. *Geophysical Research Abstracts*. 2019, 21: 1.
32. Sengör. A.M.C.; Natal'in, B.A.; Burtman, V.S. Evolution of the Altaid tectonic collage and Palaeozoic crustal growth in Eurasia. *Nature*. 1993, 364(6435): 299-307.
33. Xiao, W.J.; Windley, B.F.; Hao, J.; Zai, N.G. Accretion leading to collision and the Permian Solonker suture, Inner Mongolia, China: termination of the Central Asian orogenic belt. *Tectonics*. 2003, 22(6): 1069-1089.
34. Li, J.Y.; Wang, K.Z.; Sun, G.H.; Mo, S.G.; Li, W.Q.; Yang, T.N.; Gao, L.M. Paleozoic active margin slices in the southern Turfan-Hami basin:geological records of subduction of the Paleo-Asian Ocean plate in central Asian regions. *Acta Petrologica Sinica*. 2006, 22(5), 1087-1102.
35. Meng, Q.P.; He, Y.K.; Zhang, W.; Wu, T.R.; Zheng, R.G.; Xu, C.; Zhang, Z.Y. Time constraints on the closure of the Paleo-Asian Ocean on the northern margin of North China Craton: Evidence from Xihouhaozisyn-collisional granites in Siziwang Qi area. *Geological Bulletin of China*. 2013, 32(11): 1749-1759.
36. Yi, X.C.; Ye, G.F.; Jin, S.; Wei, W.B. Constraints on the process and mode of the Paleo-Asian Ocean closure from the lithospheric conductivity structure of the south-eastern Central Asian Orogenic Belt. *Tectonophysics*. 2022, 838: 229485.
37. Dai, J.X.; Li, J.; Luo, X.; Zhang, W.; Hu, G.; Ma, C.; Guo, J.; Ge, S. Stable carbon isotope compositions and source rock geochemistry of the giant gas accumulations in the Ordos Basin, China. *Organic Geochemistry*. 2005, 36, 1617-1635.

38. Yuan, Z.X. *On Upper Paleozoic subtle gas pools in Tabamiao District*; Chengdu University of Technology: Chengdu, China, 2005.
39. Hou, Z.S.; Chen, S.Y.; Liang, Z. Sedimentary features and sequence stratigraphy of the successions around the Carboniferous-Permian boundary in the Ordos Basin: links to glacial and volcanic impacts. *Journal of Palaeogeography*. 2023, 12(3), 358-383.
40. Li, P. W.; Gao, R.; Guan, Y.; Li, Q.S. The Closure Time of the Paleo-Asian Ocean and the Paleo-Tethys Ocean: Implication for the Tectonic Cause of the End-Permian Mass Extinction. *Journal of Jilin University (Earth Science Edition)*. 2009, 39(3), 521-527.
41. Wilhem, C.; Windley, B.F.; Stampfli, G.M. The Altaids of Central Asia: A tectonic and evolutionary innovative review, *Earth-Science Reviews*. 2012, 113, 303-341.
42. Fang, G.Q.; Liu, D.L.; Feng, J. Wave Structre in Paleozoic era of Ordos Basin and its significance in paleogeography. *Acta Sedimentologica Sinica*. 2000, 18(3), 445-448.
43. Zhang, J.; Li, J.Y.; Liu, J.F.; L,i Y.F.; Qu, J.F.; Feng Q.W. The relationship between the Alxa Block and the North China Plate during the Early Paleozoic: New information from the Middle Ordovician detrial zircon ages in the eastern Alxa Block. *Acta Petrologica Sinica*. 2012, 28(9), 2912-2934.
44. Chen, H.D.; Hou, Z.J., Tian, J. C., Liu, W. J., & Zhang, J. Q. The relationship between the Alxa Block and the North China Plate during the Early Paleozoic: study on sequence stratigraphy of deposits and tectono-sedimentary evolution in Ordos Basin during Late Palaeozoic. *Journal of Mineralogy and Petrology*. 2001, 21(3), 16-22.
45. Chen, A.Q.; Chen, H.D.; Xu, S.L.; Lin, L.B.; Shang, J.H. Sedimentary Filling of North Ordos and Their Implications for the Soft Collision Process of Hing Gan Mts.-Mongolia Orogenic Belt in Late Paleozoic. *Journal of Jilin University (Earth Science Edition)*. 2011, 41(4), 953-965.
46. Ren, Z.L. Thermal history of Ordos Basin assessed by apatite fission track analysis. *Acta Geophysica Sinica*. 1995, 38(3), 339-349.
47. Zhao, M.W.; Behr, H.J. Vitrinite reflectance in Triassic with relation to geothermal history of Ordos Basin. *Acta Petrolei Sinica*. 1996, 17(2), 15-23.
48. Yang, J.J.; Pei, X.G. *Chinese Natural Gas Geology, Volume 4, Ordos Basin*; Petroleum Industry Press: Beijing, China, 1996.
49. Wang, T.H. Structural styles of fronts of thrust-detachment faults in petroleum-bearing areas of Western China. *Acta Geologica Sinica*. 1999, 73(4), 371-383.
50. Bradley, D.R.; Andrew, D.H.; Brian, J.D.; Lynde, N.; Adrian, B. Sedimentary record of Triassic intraplate extension in North China: evidence from the nonmarine NW Ordos Basin, Helan Shan and Zhuozi Shan. *Tectonophysics*. 2004, 386, 177-202.
51. Bradley, D.R.; Amy, W.; Stephan, A.G.; Brian, J.D. Mesozoic tectonics and sedimentation of the giant polyphase nonmarine intraplate Ordos Basin, western North China Block. *International Geology Review*. 2009, 51, 95-115.
52. Hou, R.Y.; Liu, Z.Q. Reservoir evaluation and development strategies of Daniudi tight sand gas field in the Ordos Basin. *Oil & Gas Geology*. 2012, 33(1), 118-128.
53. Tan, C.X.; Li, W.H.; Zhang, H.J.; Zheng, Y. Study of the sedimentary facies of Shanxi formation in Daniudi Gasfield of Ordos Basin. *Journal of Northwest University (Natural Science Edition)*. 2011, 41(1), 107-112.
54. Wan, Y.L.; Li, Z.D.; Peng, C.; Kong, W.; Xie, Y.X.; Zheng, T. Reservoir characteristics and evaluation of low porosity and permeability sandstone of member of Shanxi Formation in Daniudi Gas Field, Ordos Basin. *Journal of Mineralogy and Petrology*. 2016, 36(3), 106-114.
55. Darby, B.J.; Ritts, B.D. Mesozoic contractional deformation in the middle of the Asian tectonic collage: The intraplate Western Ordos fold-thrust belt, China. *Earth and Planetary Science Letters*. 2002, 205, 13-24.
56. Xu, N.N.; Qiu L.W.; Eriksson, K.A.; Klyukin, Y.I.; Wang, Y.; Yang, Y.Q. Influence of detrital composition on the diagenetic history of tight sandstones with implications for reservoir quality: Examples from the Permian Xiashihezi Formation and Carboniferous Taiyuan Formation, Daniudi gas field, Ordos Basin, China. *Marine and Petroleum Geology*. 2017, 88, 756-784.
57. Yang, Y.T.; Li, W.; Ma, L. Tectonic and stratigraphic controls of hydrocarbon systems in the Ordos basin: A multicycle cratonic basin in central China. *AAPG Bulletin*. 2005, 89, 255-269.
58. Zhang, Q.; Bai, J.F.; Wang, Y. Analytical scheme and quality monitoring system for China Geochemical Baseline. *Earth Science Frontiers*. 2012, 19(3), 33-42.
59. Folk, R.L. *Petrology of Sedimentary Rocks*; Hemphill Publishing Company: Austin, USA, 1974.
60. Wang, J.W.; Bao, Z.D.; Chen, M.J.; Sun, F.J.; Liu, R.E.; Zhao, M.F.; Sun, Q.Y. Differentiation of sandstones' tuff fillings and its effect on porosity-An example from the Paleozoic sandstones in Northwestern Ordos. *Chinese Journal of Geology*. 2005, 40(3), 429-438, 456.
61. Li, X.B.; Wang, J.W. The formation and evolution of volcanic dust fillings of sandstone in coal measures strata of Ordos Basin. Acta Petrologica Et Mineralogica. 2007, 26(1), 42-48.
62. Bhatia, M.R. Plate tectonics and geochemical com position of sandstones. *Journal of Geology*. 1981, 91, 611-627.

63. Bhatia, M.R.; Crook, K.A.W. Trace element characteristics of graywackes and tectonic setting discrimination of sedimentary basins. *Contributions to Mineralogy and Petrology*. 1986, 92, 181-193.
64. Taylor, S.R.; McLennan, S.M. The continental crust: Its composition and evolution. Blackwell Scientific Publications: Oxford, UK, 1985.
65. Duan, R.H. *The nature and significance of the late Neoarchean and late Paleoproterozoic tectono-thermal events in the southern margin of the Yinshan Block of the North China Craton*; Chinese Academy of Geological Sciences: Beijing, China, 2021.
66. Jia, B.W.; Zhou, A.C.; Guo, M.T. Study on the provenance of the Late Paleozoic volcanic events in Daqingshan area. *Chinese Science Abstracts*. 1999, 5(4), 506-510.
67. Norry, M.J.; Dunham, A.C.; Hudson, J.D. Mineralogy and geochemistry of the Peterborough Member, Oxford Clay Formation, Jurassic, UK: element fractionation during mudrock sedimentation. Journal of the Geological Society. 1994, 151, 195-207.
68. Zai, Y.S.; Deng, J.; Tang, Z.L.; Xiao, R.G.; Song, H.L.; Peng, R.M.; Sun, Z.S.; Wang, J.P.; Xiang, Y.C.; Huang, H.S.; Zhang, Z.W.; Yang, L.Q.; Bai, Y.L.; Chen, C.X.; Ding, W.J.; Wang, Q.F.; Hu, L.; Xu, Z.H.; Miao, L.C.; Su, S.G.; Li, Q. *Metallogenic system of ancient land margin*; Geological Publishing House: Beijing, China, 2002.
69. Chen, B. *The U-Pb geochronology of detrital zircon and its geological significance of the Upper Paleozoic in the northeastern Ordos Basin*; Northwest University: Xi'an, China, 2020.
70. Shen, B.H.; Shen, S.W.; Wu, Q.; Zhang, S.C.; Zhang, B.; Wang, X.D.; Hou Z.S.; Yuan D.X.; Zhang Y. C.; Liu, F.; Liu, J.; Zhang, H.; Shi, Y.K.; Wang, J.; Feng, Z. Carboniferous and Permian integrative stratigraphy and timescale of North China Block. *Science China (Earth Sciences)*. 2022, 65(6), 983-1011.
71. Shao, L.; Liu, Z.W.; Zhu, W. L. Application of sedimentary geochemistry ofterrigenous classic rock to basin analysis. *Earth Science Frontiers*. 2000, 7(3), 297-304.
72. Dickinson W.R.; Suczek. C.A. Plate tectonics and sandstone compositions. *AAPG Bulletin*. 1979, 63, 2164-2182.
73. Bureau of Geology and Mineral Resources of Inner Mongolia Autonomous Region. *Regional geology of Inner Mongolia Autonomous Region, People's Republic of China, Ministry of Geology and Mineral Resources, Geological Memoirs*; Geological Publishing House: Beijing, China, 1991.
74. Jia, B.W.; Wu, Y.Q. Recognition and Geologic significance of the premo-Carboniferous volcaniclastic rocks from DaQingShan Coalfield, Inner Mongolia, China. *Scientia Geologica Sinica*. 1996, 5(4), 469-482.
75. Zhou, A.C.; Jia, B.W.; Ma, M.L.; Zhang, H. The Whole Sequences of Volcanic Event Deposits on the North Margin of the North China Plate and Their Features. *Geological Review*. 2001, 47(2), 175-183, 5.
76. Zhang, Q.; Li, Y.H.; Chen, G.C.; Han, W.; Wang, J. Geochronology, geochemistry, and Hf isotopic compositions of the Late-Carboniferous volcanic rocks in Tongshengmao of Daqinshan area, Inner Mongolia and their geological implications. *Geological Journal of China Universities*. 2018, 24(2), 160-171.
77. Jia, B.W.; Wu, Y.Q. The provenance and stratigraphic significance of volcanic event layers in Late Paleozoic coal measures from Daqingshan, Inner Mongolia. *Jour Geol & Min Res North China*. 1995, 10(2), 203-213.
78. Liu W.B.; Chen Y.T.; Wang D.Y.; Zheng C.G.; Huang G. Study on the characteristics of palaeocurrents by using dipmeter logging data. *Scientia Geologica Sinica*. 1994, 29(3), 291-297.
79. Lin, X.X. *A synthetic thought of provenance analysis in the terrigenous clastic rock basin— An example in the Lower* Permian *Shanxi Formation, Northern Ordos Basin*; Chengdu University of Technology: Chengdu, China, 2011.
80. Li, J.Y. Permian geodynamic setting of Northeast China and adjacent regions: closure of the Paleo-Asian Ocean and subduction of the Paleo-Pacific Plate. *Journal of Asian Earth Sciences*. 2006, 26, 207-224.